

QUANTIFYING MOSS RESPONSE TO CONTAMINANT EXPOSURE USING
LASER INDUCED FLUORESCENCE

A THESIS SUBMITTED TO THE GRADUATE DIVISION OF THE
UNIVERSITY OF HAWAI‘I AT MĀNOA IN PARTIAL FULFILLMENT
OF THE REQUIREMENTS FOR THE DEGREE OF
MASTER OF SCIENCE
IN
EARTH AND PLANETARY SCIENCE
DECEMBER 2020

By
Kelly Truax

Thesis Committee:
Henrietta Dulai, Chairperson
Anupam Misra
Wendy Kuhne

Keywords: Moss, Bryophyte, Copper, Metal Contamination, Environmental
Contamination, Metal Detection, Laser Induced Fluorescence

ACKNOWLEDGEMENTS

A special thanks goes to my committee members: Drs. Henrietta Dulai, Anupam Misra, and Wendy Kuhne. They have provided a wealth of knowledge and many an idea for current and future endeavors. Asking questions that broaden not only my understanding, but my approach to research makes each of them invaluable. I'd like to extend extra thanks to my advisor Henrietta who was always a second mind to any of my thoughts, who challenged me to rework and revise everything, and who struggled with me to see this research through to the end. Thanks to Anupam for allowing me unfettered access to the laser and constant ideas on new ways of testing and interpreting the results. Thanks to Wendy for asking wonderful questions, being full of energy and excitement, and constantly giving me ideas for what comes next.

To Dr. Garrett Apuzen-Ito for his assistance and expertise in data analysis; thanks for being a second eye and making great suggestions. To Dr. Paul Lucey for pointing me in different directions for my analysis and opening new thought processes for future work. To Henrietta's family for all their smiles and help with statistics. To Dr. Clifford Smith for his help regarding bryophytes and identifying species of interest. Thanks to Carrie Tome and the Microbiology Department. The decommission of their lab spaces and coordination with Carrie was paramount to obtaining equipment that directly helped my research and sample transport.

Thank you also goes to the Savannah River National Laboratory to Drs. Wendy Kuhne and Laura Tovo for their support and collaboration on testing/application of the Biofinder. To friends and family who have listen to me rant about moss for the last year. And of course, to MTV's collaboration with which none of this work would be possible. This project is funded through the Department of Energy Consortium for Monitoring Technology and Verification in collaboration with the University of Michigan.

ABSTRACT

The project goal was to develop a detection method of biological response to metal contamination in mosses using a non-destructive laser induced fluorescence (LIF) technique. Moss was selected due to its long history of use in tracing atmospheric deposition of heavy metals and nuclear fallout. Increasing treatments of copper chloride (CuCl_2) ranging from .035 to .100 mg/cm^2 were administered to three moss samples every 48 hours until reaching a total of 5 doses (10 days). Moss fluorescence was used as a measure of biological response to Cu and was measured using LIF from 532 nm green and 355 nm UV lasers. Images of LIF response were captured using a CMOS camera and red-green-blue (RGB) decimal code values were extracted for each pixel in the images. Pixel densities of color channels from treated and untreated moss samples were compared revealing a shift to lower decimal codes in red and green densities with increase in Cu. The data also suggests that Cu applied as a single dose or in multiple smaller increments over time induce the same response. Multiple quantitative analyses of color distributions were used to demonstrate that LIF is a viable method to identify biological response to Cu in moss at mg/cm^2 Cu levels. As such, LIF shows great promise for environmental remote sensing applications.

TABLE OF CONTENTS

ACKNOWLEDGEMENTS	ii
ABSTRACT	iii
TABLE OF CONTENTS	iv
LIST OF TABLES	v
LIST OF FIGURES	vi
LIST OF ABBREVIATIONS	vii
PREFACE	viii
1. Introduction	1
2. Methodology	3
2.1. <i>Laboratory Treatment of Moss with Metals and Analysis of Metal Concentration</i>	4
2.2. <i>Laser Induced Fluorescence Imaging</i>	6
2.3. <i>Data Analysis</i>	7
3. Results	9
3.1. <i>Qualitative Description of LIF Image Color Components</i>	9
3.2. <i>Quantitative Analysis of LIF Image Color Components</i>	17
3.2.1. <i>Interpreting Trends</i>	17
3.2.2. <i>Single color overlap and difference analysis</i>	18
3.2.3. <i>Single color pattern analysis</i>	20
3.2.4. <i>Two color pattern analysis</i>	30
3.2.4. <i>48-hour analysis</i>	34
4. Discussion	36
5. Conclusion	39
Appendix A	40
A.1 <i>Documentation of LIF – Misra (Biofinder)</i>	40
A.2 <i>Moss Species Selection</i>	41
A.3 <i>Moss Cultivation</i>	43
Appendix B – Normalization plots	44
Bibliography	46

LIST OF TABLES

Table 1.....5
Table 25
Table 3 21
Table 422
Table 523
Table 625
Table 727
Table 8 28
Table 9 29
Table 10 30
Table 11 31
Table 12.....33
Table 13.....33
Table 14.....35
Table 15.....35

LIST OF FIGURES

Figure 1:	2
Figure 2:	3
Figure 3:	6
Figure 4:	7
Figure 5:	8
Figure 6:	11
Figure 7:	12
Figure 8:	13
Figure 9:	14
Figure 10:	15
Figure 11:	16
Figure 12:	17
Figure 13:	18
Figure 14:	19
Figure 15:	20
Figure 16:	21
Figure 17:	24
Figure 18:	26
Figure 19:	30
Figure 20:	31
Figure 21:	32
Figure 22:	34
Figure A-1	40
Figure A-2	40
Figure A-3	41
Figure A-4	41
Figure A-5:	42
Figure B-1:	44
Figure B-2:	45

LIST OF ABBREVIATIONS

Biofinder – Standoff Biofinder; developed by Misra et al. (2018) for future NASA missions to remotely detect biological materials. It uses a 532nm green laser and 355nm UV laser that fire in tandem at nanosecond pulses. It is designed to use nanosecond laser pulses with a compact color CMOS camera as the detector to collect time-resolved images (Misra et al., 2018). The Biofinder is the primary technology used to quantify use of LIF in metal accumulation in biota.

DOE – U.S. Department of Energy

CL – Expresses the difference between two curves by comparing points along the x-axis by their individual ratios respective of the length of the overall curve. Similar to Euclidean distance.

CMOS – Complementary Metal Oxide Semiconductor camera with transistors at every pixel translating light to electrons using about 100x less power than a CCD camera. Though more cost effective, they have less light sensitivity and are more susceptible to the introduction of noise.

Cu – copper

CuCl₂ – copper chloride

DI – deionized water

DTW – Dynamic Time Warping; method for finding the distance between two curves and calculating the path that minimizes the cumulative distance between those points

EPA – U.S. Environmental Protection Agency

LIF – laser induced fluorescence; the technique of using a laser to excite particles which release energy when they return to a stable state which appears in different wavelengths of light

MTV – Consortium for Monitoring Technology and Verification (University of Michigan)

Nd:YAg – Neodymium-doped yttrium aluminum garnet crystal (Nd:Y₃Al₅O₁₂) that is used as a lasing medium for solid-state lasers.

NNSA – National Nuclear Security Administration

RGB – red-green-blue; specifically, in reference to color spectrum or decimal codes as they pertain to red, green, and blue color channels.

PREFACE

The research conducted for this thesis is the direct result of funding provided by a grant from the Department of Energy (DOE) and the National Nuclear Security Administration (NNSA). The overarching grant is led by the Consortium for Monitoring, Technology, and Verification (MTV) at the University of Michigan. MTV was founded to develop methods focused on detecting and deterring nuclear proliferation through the three thrust areas: monitoring, technology, and verification. The research described here falls under the branch of new technological developments. More specifically, our objective is to develop technology targeted at biota to detect contamination from nuclear fallout, waste products from mining and other nuclear fuel cycle and uranium purification processes.

The focus of this research is to take advantage of biota that record chemical signatures from their environment and use their response to such exposure as indications of the presence of metals or chemicals of interest without the need for sample collection and ex-situ chemical analysis. The work detailed in this Thesis is a proof of concept and will be built upon in future steps of the project. Moss was used as a viable environmental monitor of chemical change in tandem with a newly developed remote sensing technique based on laser induced fluorescence called the Standoff Biofinder (LIF; Misra et al., 2018). Future work will aim to investigate other metals and radionuclides, field and drone applications, viability of microscope laser methods, and application to other types of biota.



1. Introduction

Since the 1960's, bryophytes have been one of the most frequently utilized biological systems for monitoring heavy metal pollution (Tremper et al. 2004). While some naturally-occurring metals are important for biological organisms, in excess heavy metals or radionuclides can have dire effects on metabolic functions in biota leading to physiological stress (Nagajyoti et al., 2010; Krzesłowska, 2011). Due to bryophytes having relatively simple biology, they have been suggested as ideal organisms for observing genetic or morphological changes linked to metal toxicity (Carginale et al., 2004; Coudhury & Panda, 2005).

Mosses are a type of bryophyte (Clade: Embryophyta, Division: Bryophyta) that lack a true root system leading them to absorb heavy metals across their surface (Berg & Steinnes, 1997; Degola et al., 2014). Metal ions interact easily with the cell walls of moss due to a lack of a cuticle layer (Choudhury & Panda, 2005; Koz & Cevik, 2014) and their large surface-to-weight ratio (Sun et al., 2009). Moss' tissue structure allows for more rapid uptake and physiological response to changes in heavy metal concentrations in comparison to vascular plants (Zvereva & Kozlov, 2011). Their less specialized connecting tissue (Onianwa, 2001) and slow growth rate (Chakraborty & Paratkar, 2006) means that moss can integrate metals from short-term events and retain a longer history of exposure. Monitoring using moss has been successfully implemented over decades in terrestrial and aquatic environments leading to a wide range of applications. Mosses are also one of the most robust and resilient plant species persisting in even the harshest environments (Reski, 1998).

Due to the resiliency of mosses, stunted growth is often a difficult parameter to observe in metal toxicity studies. However, alterations in chloroplasts (Choudhury & Panda, 2005), and total chlorophyll content have been documented in conjunction with heavy metal dosing experiments (Tremper et al., 2004; Sun et al., 2009). Of the metals tested, copper (Cu) was consistently found to cause measurable decline in chlorophyll, while also increasing chlorophyll-b to chlorophyll-a ratios (Shakya et al., 2008). For these reasons, and the metal's natural uptake by plants, Cu was selected in this study.

Metals distributed through the atmosphere can be delivered via dry fallout, precipitated onto the surface of terrestrial bryophytes by wet deposition, and during wet seasons through runoff (Berg et al., 1995; Berg & Steinnes, 1997; Wolterbeek, 2002; Stankovic, J.D., 2018). The retention of particles on a moss' surface is largely dependent on the size of the moss and the lipid structure of the cell walls (Chakraborty & Paratkar, 2006). Metal accumulation can occur through several mechanisms but reversible adsorption on the cell surface can be the greatest limitation to metal mobilization within the organism (González & Pokrovsky, 2014). Adsorbed metals can be dissolved in solution, trapped as particulate matter on the surface, deposited in surrounding cells, bound to chelating sites, or transported inside cells (Vázquez et al., 1999).

Thanks to their bioaccumulating capacity mosses are cost effective biomonitors, but their large-scale sampling and testing can still become expensive and laborious. There is room for less invasive, in-situ detection methods and technology that may complement or replace traditional sampling. One such technique is being explored in this paper and employs laser induced fluorescence. Laser induced fluorescence (LIF) is an emerging spectroscopic and imaging

technique that documents changes in atomic energy level. Atoms or molecules are excited to a higher energy level after absorption of electromagnetic radiation from a laser and respond with spontaneous emission of light, deemed fluorescence (Kinsey, 1977; Maarek & Kim, 2001). Compared to absorption spectroscopy, LIF has better detection sensitivity and high signal-to-noise ratio (Zare, 2012). Near-IR (infrared) spectroscopy is a currently employed technique in agriculture due to its ability to be non-destructive, accurate, and inexpensive. However, the higher wavelengths can result in reduced sensitivity leading to constraints on distance from samples and position of the sun when imaging (García-Sánchez et al., 2017; Tan et al., 2019).

The technology used in this work is the “Standoff Biofinder” (Biofinder) developed by Misra et al. (2018) to remotely detect biological materials. It uses a 532 nm green laser and 355 nm UV laser that fire in tandem at nanosecond pulses (112 ns). The rate of fire was selected due to most biogenic and organic materials showing a short lifetime fluorescence (<20 nanoseconds) from laser sources in the wavelength ranges used. The benefit of using the 532 nm laser comes from its ability to observe, for example, chlorophyll which has emission in the red region. The 355 nm laser focuses on emission in the blue region which is sensitive to microbial activity and hydrocarbons. The Biofinder is designed to use nanosecond laser pulses synced with a compact color complementary metal oxide semiconductor image sensor (CMOS) camera as the detector to collect time-resolved images (Misra et al., 2018). This paper explores biological imaging using the Biofinder, which represents a new technology that shows promise in capabilities of quantifying changes in emissions in biological material as a response to metal toxicity. This work builds on extensive evidence of moss aptly accumulating metals (Tremper et al., 2004) from atmospheric fallout (Berg & Steinnes, 1997), previously documented physiological changes such as shifts in chlorophyll composition from metal uptake (Choudhury & Panda, 2005; Shakya et al., 2008; Krzesłowska et al., 2013), and the promise of LIF to identify these well documented processes through non-invasive techniques.

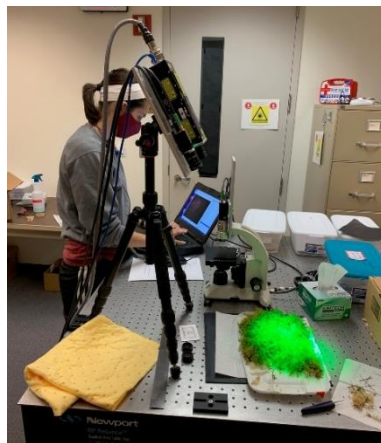


Figure 1:
Biofinder imaging of moss

2. Methodology

The moss species selected for experimentation was a frond-like moss *Thuidium plicatile*, which is endemic to Hawai'i (Staples et al., 2004). The research was divided into three parts that focused on a methodology to detect moss responses to metal exposure. Part one focused on laboratory metal treatment of moss samples. Part two utilized LIF to record images with RGB values that were used to quantify moss response to the level of metal exposure. Images collected were then processed and the data were analyzed in part three for comparison of moss color change between treated and untreated samples.

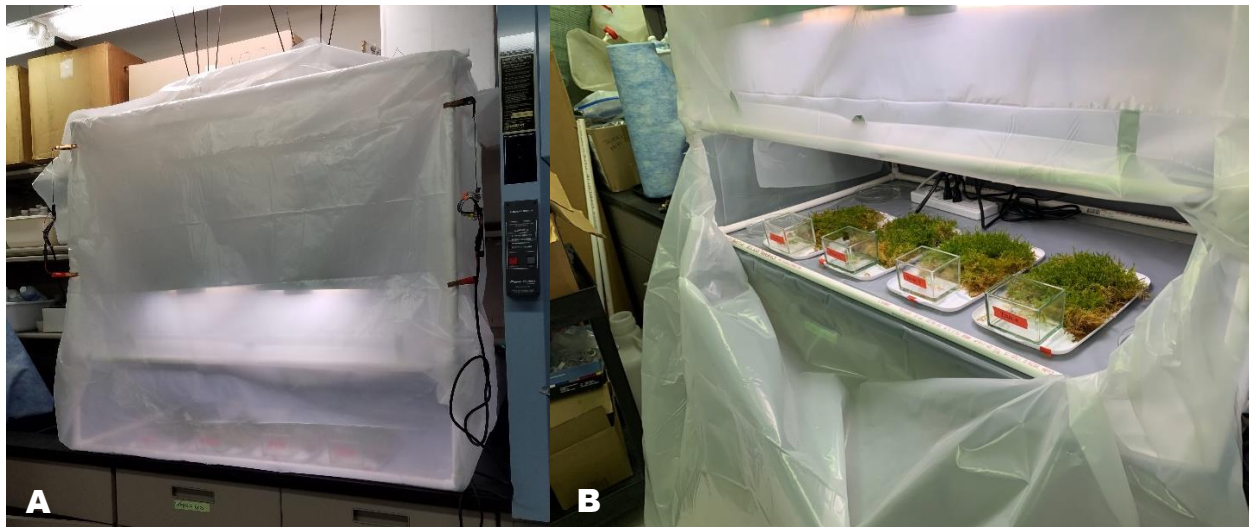


Figure 2: Before and throughout the experiment the moss samples were incubated in a controlled environment (temperature, light, humidity) grow tent constructed from PVC pipes and plastic sheets. A) Grow tent closed B) Grow tent open showing two full spectrum LED lights fixed 0.5 m above the moss samples with a day/light cycle of 10h/14h.

2.1. Laboratory Treatment of Moss with Metals and Analysis of Metal Concentration

A moss sample (*Thuidium plicatile*) was collected from a single mat along the Wa'ahila Ridge Trail and State Recreational Area beneath Cook Island Pine trees (21.307°, -157.797°) on June 1, 2020. This area transitions into forest along the Southeastern part of the Ko'olau mountain range beneath the Honolulu Watershed Forest Reserve and represent a relatively uncontaminated environment. The sample was separated onto four different trays with each patch of moss having an area of 316 cm² (7 in x 7 in). Samples were incubated in a grow tent for one week before treatment to avoid a physiological response from change in environment after their transition from the field to the grow tent. Moss samples were cultivated at a room temperature of 18-20°C, 50-60% relative humidity, and 14-17 W/m² ambient light (1400-1800 lux), with a day length of 10 hours. During the treatment period, moss was removed from the tent for about 0.5 hours for treatment and imaging after which it was immediately returned. Moss was watered with 30 ml of distilled water (DI) or Cu enriched DI water every morning before imaging throughout the duration of the experiment. DI was used to ensure that any moss response recorded was the result of Cu and not from nutrient introduction or other metals found naturally in the local Hawai'ian groundwater.

Tray 1 served as a control while the other three trays were exposed to varied levels of metal contaminant concentrations. Cu was selected as a contaminant because of its well documented biotoxicity. Moss is often commercially controlled through the application of copper sulfate (CuSO₄) in a solution of 3.8 to 9.4 g/L for every 93 square meters (Ryan, 1977). Based on initial experiments with the Biofinder it was determined that Cu doses as low as 0.00015 mol/316 cm² would induce observable changes in the moss emission color. Levels closer to 0.0005 mol/316 cm² were found to produce more conclusive changes. Accordingly, cumulative concentrations of 2.5 mM, 5.0 mM and 7.5 mM of Cu were selected for the three treatment levels. To induce gradual changes in the moss, each concentration was administered every odd day at 1/5th its potency (0.5 mM, 1.0 mM, and 1.5 mM) for 10 days reaching the desired toxicity by the end of testing. These values were converted into grams of CuCl₂ for the sample area (316 cm²) with the ideal 1/5th dose for each trial calculated as 0.0229 g, 0.0458 g, and 0.0686 g). Table 1 reflects the actual values of grams of Cu measured for each dose of each trial (0.0108 g, 0.0217 g, and 0.0324 g). The incremental dosing allowed for the monitoring of the moss' gradual response to the metal at different concentration levels. Each tray received 30 mL of DI or DI+Cu every morning before imaging using a spray bottle to simulate atmospheric wet deposition. The time steps of incremental and cumulative copper concentrations added on each sample can be seen in Table 2.

Table 1. Copper doses applied via 30 mL solution in 4 trials to four moss samples each having an area of 316 cm². Dose is specified per sample and per cm² in 1/5th and cumulative dose. The values in the table are calculated based on Cu in grams and not the original total CuCl₂ mass.

Trial	1/5 th Dose	1/5 th Dose	Total 5 Doses	Total 5 Doses	1/5 th Dose	Total 5 Doses	Total 5 Doses	Total 5 Dose
	mg/spl	mmol/spl	mg/spl	mmol/spl	mg/cm ²	µmol/cm ²	mg/cm ²	µmol/cm ²
1	0	0	0	0	0	0	0	0
2	10.815	0.170	54.077	0.851	0.034	0.539	0.171	2.693
3	21.633	0.340	108.165	1.702	0.069	1.077	0.342	5.387
4	32.436	0.510	162.179	2.552	0.103	1.615	0.513	8.076

Table 2. Experimental doses of metal added each day and cumulative concentrations of Cu reached by that day of the experiment [mg/cm² and µmol/cm²]. Numbers indicate mg or µmol Cu per cm² and the number in parenthesis indicates cumulative metal concentration added by that day. Light gray shading indicates treatment days.

Individual and Cumulative Cu dose in mg/cm²										
Day	1	2	3	4	5	6	7	8	9	10
Trial 1	0(0)	0(0)	0(0)	0(0)	0(0)	0(0)	0(0)	0(0)	0(0)	0(0)
Trial 2	.034(.034)	0(.034)	.034(.068)	0(.068)	.034(.102)	0(.102)	.034(.136)	0(.136)	.034(.170)	0(.170)
Trial 3	.069(.069)	0(.069)	.069(.138)	0(.138)	.069(.207)	0(.207)	.069(.276)	0(.276)	.069(.345)	0(.345)
Trial 4	.103(.103)	0(.103)	.103(.206)	0(.206)	.103(.309)	0(.309)	.103(.412)	0(.412)	.103(.515)	0(.515)
Individual and Cumulative Cu dose in µmol/cm²										
Day	1	2	3	4	5	6	7	8	9	10
Trial 1	0(0)	0(0)	0(0)	0(0)	0(0)	0(0)	0(0)	0(0)	0(0)	0(0)
Trial 2	0.54(0.54)	0(0.54)	0.54(1.08)	0(1.08)	0.54(1.62)	0(1.62)	0.54(2.16)	0(2.16)	0.54(2.70)	0(2.70)
Trial 3	1.08(1.08)	0(1.08)	1.08(2.16)	0(2.16)	1.08(3.24)	0(3.24)	1.08(4.32)	0(4.32)	1.08(5.40)	0(5.40)
Trial 4	1.62(1.62)	0(1.62)	1.62(3.24)	0(3.24)	1.62(4.86)	0(4.86)	1.62(6.48)	0(6.48)	1.62(8.10)	0(8.10)

2.2. Laser Induced Fluorescence Imaging

Each bulk moss was imaged before the first treatment (day-0) to provide a baseline control associated with each trial. On treatment days, moss masses on trays were imaged before and after wet treatment, and imaging continued for a 6, 12, 24, 36, and 48-hour time interval after treatment (Figure 3a). Non-treatment days resulted in DI application before the 24-hour imaging. Imaging sessions were staggered 30 minutes in order of trial number and were held consistently for each sample beginning between 7 and 9 am. Images were collected with the Baumer Camera Explorer software which allows the CMOS camera to be synchronized with the 112 ns pulses of the Nd:Yag laser. Baumer Camera Explorer allowed for the adjustment of the camera's exposure, gain, and time delay (Figure 3b; Misra et al., 2018). Images were taken at 5 gain levels based upon the laser(s) being used to optimize the captured fluorescence response. If both lasers or just the green laser was in use then the gain levels were collected at 10, 20, 30, 40, and 50. The UV laser images were collected at gains of 50, 100, 150, 200, and 250 (max gain). Images captured the same area of the moss samples every day and the moss covered the full extent of the image. Each image recorded was then processed to extract the RGB values for each pixel.



Figure 3:
(A) Adjusting focus and changing filters for individual laser analysis. (B) Controlling exposure and gain and recording the image captured.

2.3. Data Analysis

It is hypothesized that physiological changes in the moss samples from copper exposure can be captured using LIF and observed by shifts in the distribution of RGB values. The RGB values for each pixel from images collected using the Biofinder were extracted using MATLAB® and then separated by color (R, G, or B). The decimal codes for each separate color were used to create histograms of the abundance of each color channel at each point along the RGB decimal code (0-255). A histogram displays data based on frequency and is used here to find the abundance of each decimal code value. In Figure 4, various gain levels are shown in density histograms (pixel counts scaled by the inverse of the total density distribution) representing the relative pixel abundance of red, green, and blue channels based on decimal code.

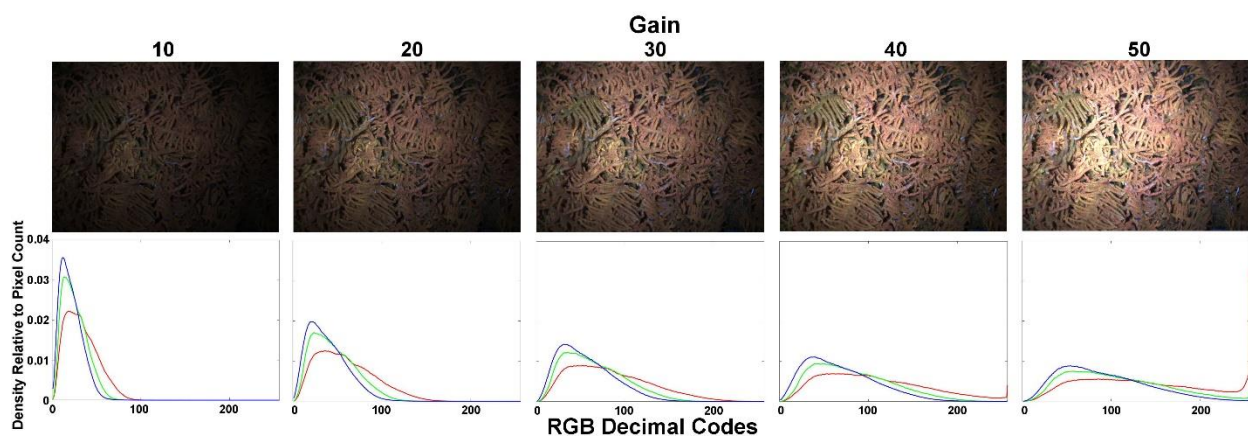


Figure 4: Density histograms (pixel count scaled by the inverse of the total density distributions). (Top) Images of 5 gain levels collected from the day-0 control sample using both lasers. (Bottom) Histogram profiles of the relative abundance of each RGB decimal code value found in each of the images. (255,0,0) is the decimal code for red, (0,255,0) is the decimal code for green, and (0,0,255) is the decimal code for blue. Code (0,0,0) would be absolute black and (255,255,255) absolute white.

Lower and higher gain levels produce under- or over saturated images and result in loss of sensitivity. In lower gain images, e.g. 10 and 20 in Figure 4, densities are not well distributed above the 100 decimal code range. Low or lack of values represent the absence of color at those decimal codes meaning there is no data to analyze or compare between samples. Higher gains of 40 and 50 are over-saturated and have “flat” shapes with excess abundance in the red color channel at the maximum decimal code (255). The gain of 30 was found to be a good balance and was selected for final data analysis for all trials. RGB density histograms from images collected at gain 30 were generated for trial 1 as a control and treated samples for corresponding days. Trials were compared to observe differences in color channels in response to metal doses applied to samples.

The next step was to determine the application and use of each laser in the Biofinder. Cu has been previously documented to cause a reddish-orange coloration response in moss when using LIF techniques (Yang-Er et al., 2019) suggesting the green laser, which picks up the red spectrum, would be the method of choice. The UV laser, however, is more sensitive to the blue

spectrum and believed to be less descriptive for the metal of interest. Density profiles for both lasers, and then separately the green laser and the UV laser can be observed in Figure 5 at a gain of 50 (lowest for UV). Densities from the image produced with the UV laser only have a right skewed shift below the 100-decimal code with red being most skewed. Though higher gains were recorded with the UV, there were no corresponding images taken with both lasers for comparison. The green laser, however, has a more even distribution and shows a well distributed red channel without significant loss of green or blue. Therefore, the green laser histograms will be included, but the UV laser will not be explored in depth in this paper.

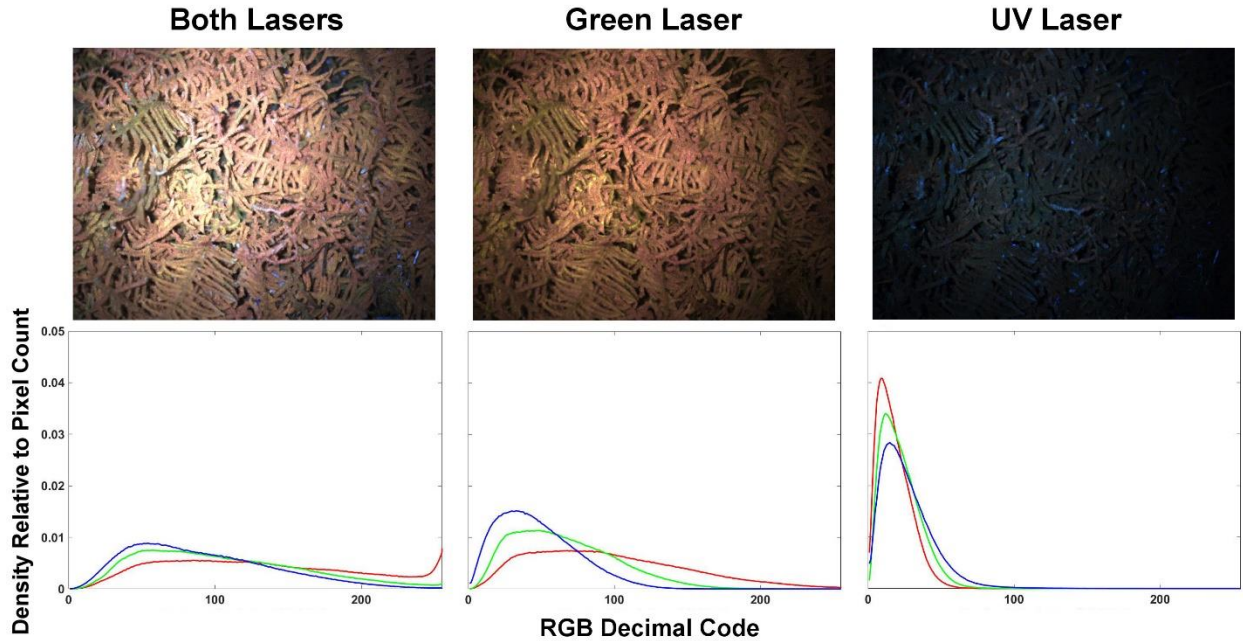


Figure 5: (Top) Images taken by the 3 laser modes: both lasers applied, green only, and UV only, respectively. Single laser images are achieved with the use of filters. (Bottom) Histogram profiles of the relative abundance of each RGB decimal code value found in each of the images which were collected at a gain of 50. Red and green channels can be seen dominantly in the green laser which contributes heavily to the profile observed for both lasers. Though red and green are present when using the UV laser, the blue channel is dominant.

3. Results

3.1. Qualitative Description of LIF Image Color Components

Density histograms showing frequency distributions of color decimal codes normalized by total number of counts were produced for each sample for each day using images taken using both lasers (Figure 6) and the green laser only (Figure 7). The histograms from both lasers show the control, trial 1, generated reproducible distribution profiles with minor fluctuations (e.g. day 4) in R, G, and B colors over the 10 days. Deviation in all trials can be seen on day 4 though no change in the growth tent conditions were noted through duration of the experiment. For trials 2, 3, and 4, the general trend follows an overall reduction in red and green color frequency distribution while the blue color seems less variable over the 10-day course of the experiment. For the images produced by the green laser only, decimal color code density histograms show red color having the highest frequency followed by green and blue colors. On images of moss subjected to higher Cu doses, the green color frequency tends to decrease to levels resembling blue decimal code distributions. One notable difference in green laser images compared to both lasers is that color histograms do not extend the full 0-255 range with lighter, higher decimal code values underrepresented. To visualize the difference between trials, treated samples were compared to the trial 1 control for metal induced difference.

Normalization of trials 2, 3, and 4 to the control, trial 1, was performed by dividing the values in corresponding color decimal codes in treated trials by the controls. All control normalized treated trials in general show ratios decreasing below 1 for all 3 colors as the experiment progresses (Appendix B; Figure B-1). By day 7 all colors in all treated trials plot below 1. Green laser observation (Appendix B; Figure B-2) shows the control normalized treated samples being above the ratio of 1 initially (1-4 days) then falling below 1 as the experiment continues. Control normalization is also affected by the color histograms not extending the full 0-255 range, especially for the green and blue colors. The change in red channel appears between each day of the experiment and shows a similar shape on each day of the experiment regardless of trial or dose. This could indicate that the change in green channel in normalizations is just as descriptive of toxicity while the red channel is more useful in histograms. Moreover, the relationship between the two regardless of method could be a good indicator of toxicity.

Different rates of change in red and green channels with applied metal concentration in the histograms suggest that the relationship between the red and green channels may be a means of quantifying differences between treated trials and the control. The red and green profiles were extracted from images and the pixel counts were scaled by the inverse of the total density distribution and plotted against each other. This was repeated for each trial compared to the control and the profiles for all trials were stacked for each day (Figures 8 & 9). Applying both lasers reveals that trial 4 is different from the trial 1 control from the first day of testing. For trials 2 and 3 it takes multiple days to depart from the control but eventually all trials show differences. Green laser plots (Figures 10 & 11) are quite similar but take longer for the profiles to distinguish themselves from the control.

The advantage of this approach is that it takes information from two colors to observe their relationship and co-evolution over time. Both red and green color densities have the same scale (decimal code ranging from 0-255) and the same fixed pixel count densities, i.e. normalized to 1. Since the total number of pixels is the same, only the shape of the densities differs based on changes in the relationship between red and green channels. The difference in these shapes between images is responsible for the loop shape illustrated in Figures 8 and 9. The point on the loop farthest from the origin, or apex, is represented by the peak values of the densities and so is driven by how “peaked” or right skewed the densities are. It is apparent that the modes shift left over the 10 days of the experiment in treated samples which manifest as longer loops in Cu dosed trials with increased toxicity. The green to red color comparison is explored further by quantifying differences in loop shapes with various treatment levels.

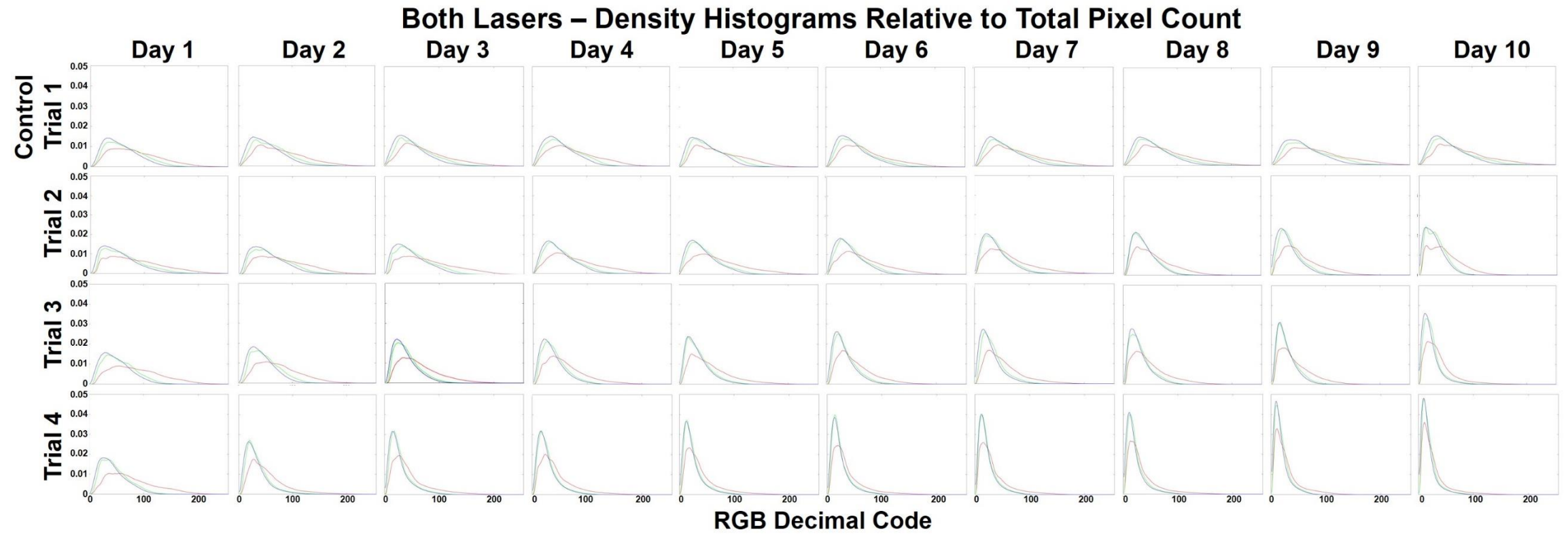


Figure 6: Density histogram profiles (both lasers) of moss LIF images separated by color channel and plotted for abundance at each RGB

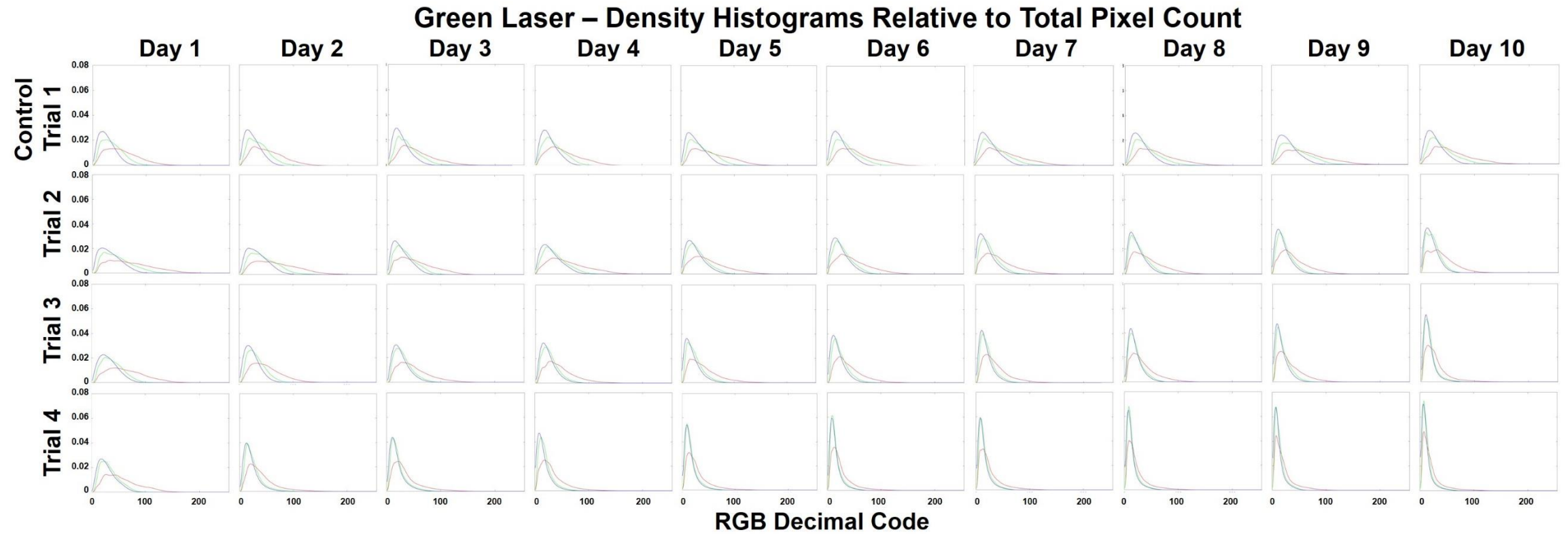


Figure 7: Density histogram profiles (green laser only) of moss LIF images separated by color channel and plotted for abundance at each RGB decimal code.

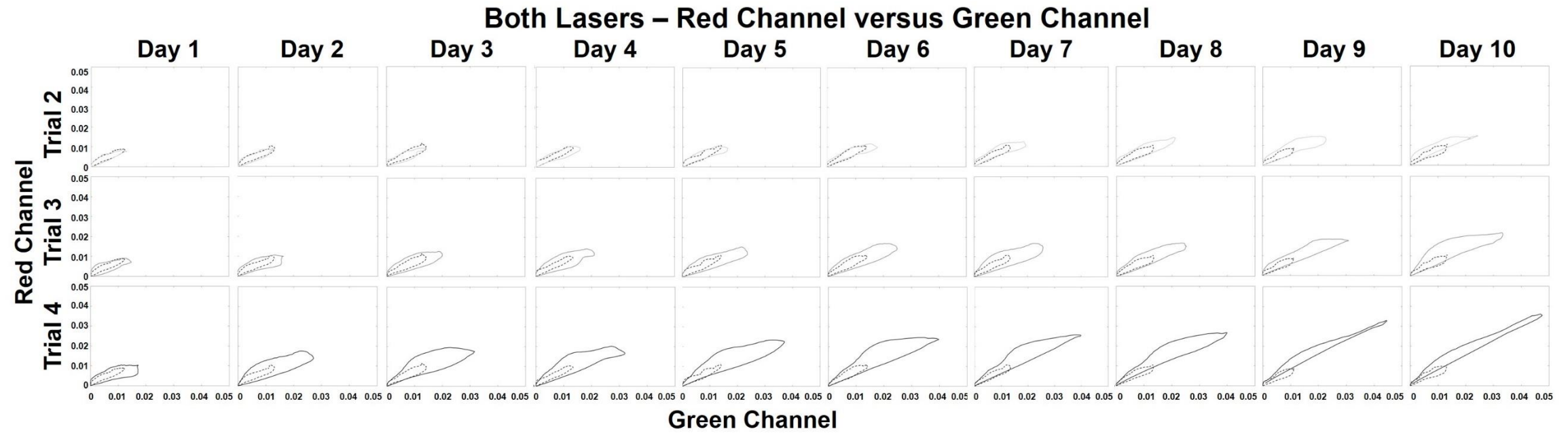


Figure 8: Red versus Green plots (both lasers) using color channels generated from initial images and their histogram profiles (Figure 6). From darkest to lightest: dashed black is trial 1 (control), light gray is trial 2, medium gray is trial 3, and dark gray is trial 4. Profiles are plotted for each day to compare each trial's potential deviation from the control.

Both Lasers - Red vs Green Profiles Stacked for all Trials

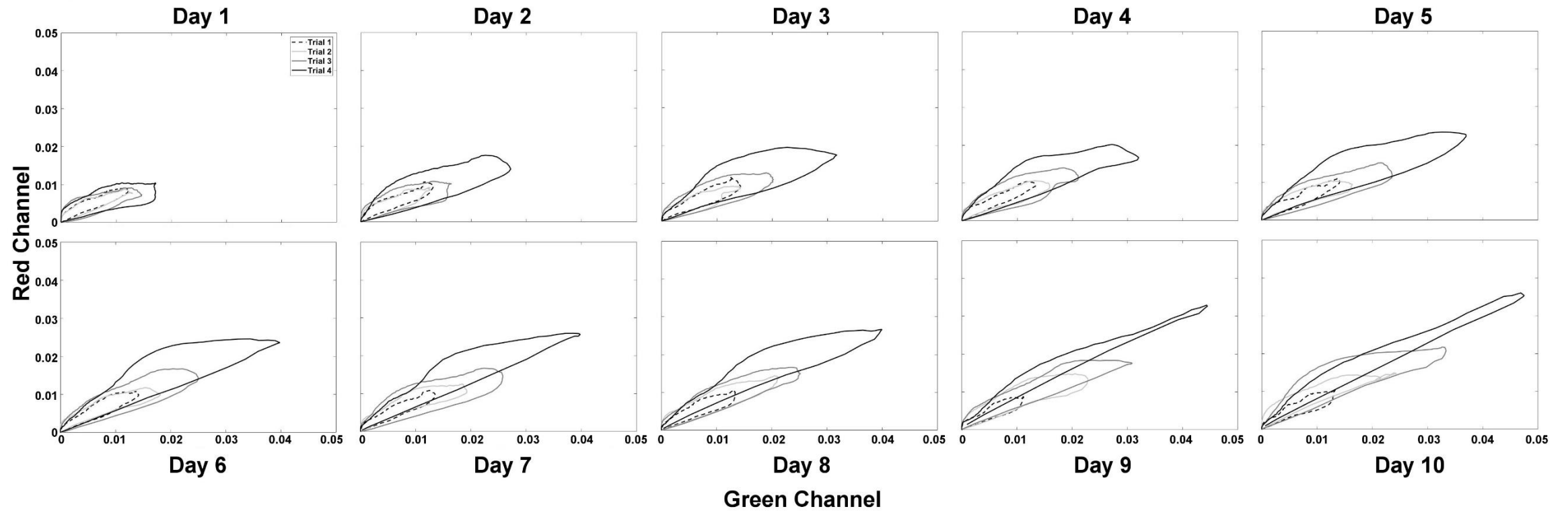


Figure 9: Stacked Red versus Green plots (both lasers) using color channels generated from initial images and their histogram profiles (Figure 6). From darkest to lightest: dashed black is trial 1 (control), light gray is trial 2, medium gray is trial 3, and dark gray is trial 4. Profiles are plotted for each day to compare each trial's potential deviation from the control.

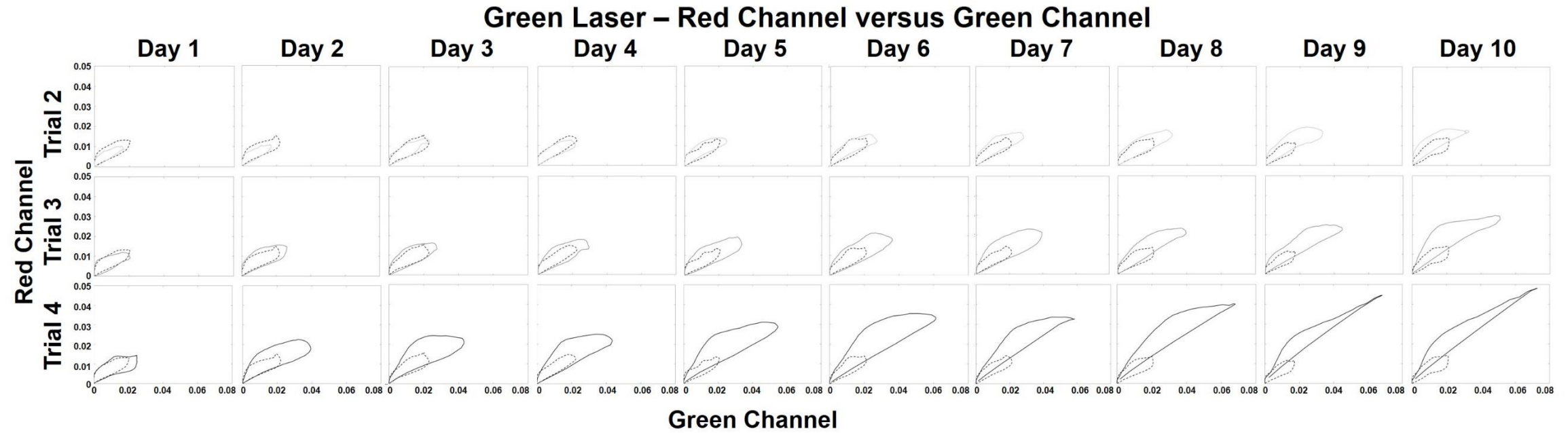


Figure 10: Red versus Green plots (green laser only) using color channels generated from initial images and their histogram profiles (Figure 7). From darkest to lightest: dashed black is trial 1 (control), light gray is trial 2, medium gray is trial 3, and dark gray is trial 4. Profiles are plotted for each day to compare each trial's potential deviation from the control.

Green Laser - Red vs Green Profiles Stacked for all Trials

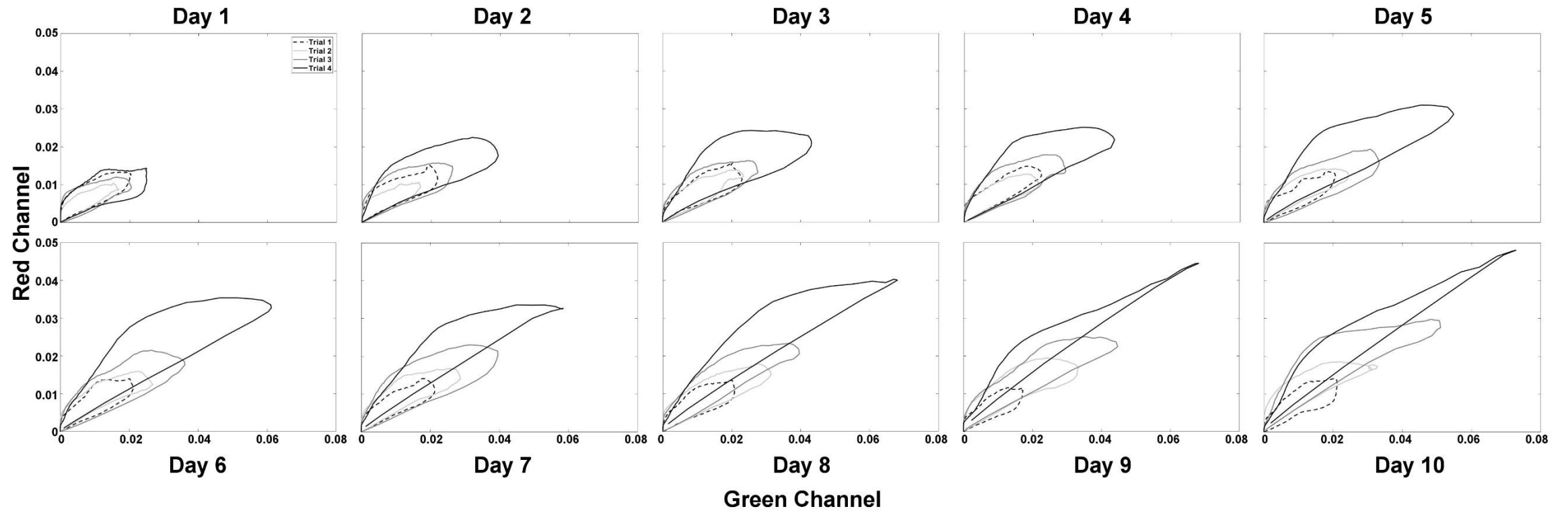


Figure 11: Stacked Red versus Green plots (green laser only) using color channels generated from initial images and their histogram profiles (Figure 7). From darkest to lightest: dashed black is trial 1 (control), light gray is trial 2, medium gray is trial 3, and dark gray is trial 4. Profiles are plotted for each day to compare each trial's potential deviation from the control.

3.2. Quantitative Analysis of LIF Image Color Components

3.2.1. Interpreting Trends

Plots of color distribution in images of the bulk moss samples expressed as density histograms, normalizations to the trial 1 control, and red to green plots for both lasers, and the green laser alone, suggest that LIF could potentially be used to show that a moss sample has been exposed to Cu. It becomes necessary, then, to explore different ways to quantitatively express these observed changes in images of the moss exposed to Cu. It is also of interest to determine the lowest threshold of detection identifiable using the LIF technique. The histogram plots more clearly show a reduction of higher decimal code values in the red and green channels for all trials (with the blue staying stable as metal toxicity increases). Figure 12 shows the sum of RGB decimal codes for all trials plotted together. At day 1, all samples appear similar, save trial 4, but over time the treated samples shift to higher abundance in lower decimal codes (darker image). By day 10, all trials have most of their point counts shifted to within 0-50 but the control (black dashed line) is unchanged. Color heat maps and color separated histograms (Figure 13) were created for the last day of the experiment (day 10) to qualitatively demonstrate this color shift, or “darkening” in decimal code having higher densities on the left side of histograms.

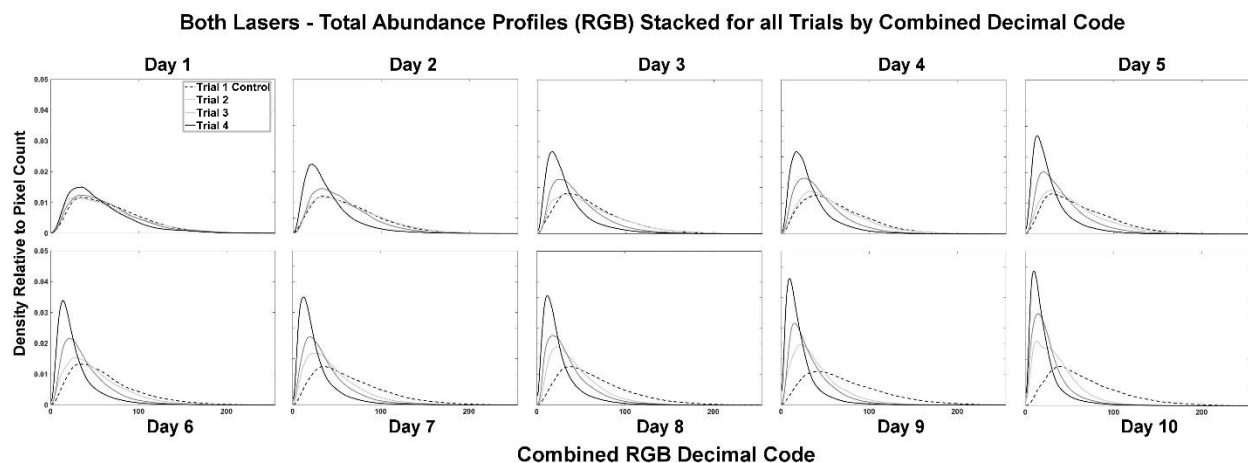


Figure 12: Combined RGB decimal code values for each trial and day. Dashed black line is trial 1 control and darkest solid line is trial 4. General narrowing and heightening trend are observed for all treated samples in comparison to the control.

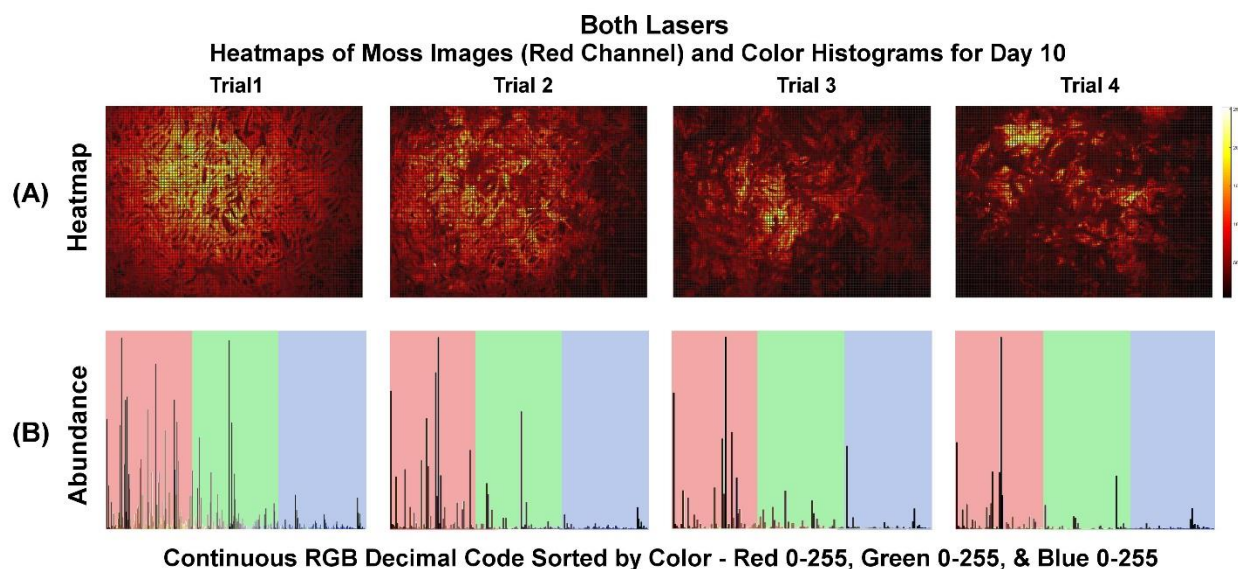


Figure 13: (A) The red channel of images collected with the Biofinder. The resolution of the images was reduced to 10% of their original size for easier analysis (150x200 pixels). Yellows represent the highest decimal codes while black the lowest. (B) Abundance of red, green and blue colors in the trials plotted in R,G,B order from 0-255

3.2.2. Single color overlap and difference analysis

One way to assess differences and similarities between color distribution of different images is to quantify the points of intersection of two curves. This information can then be used to find the overlap or difference of each color histogram or density (Figure 14). Densities for each color channel from the control (trial 1) and treated trials 2,3,4 were compared to their respective day-0 color densities for each day over the course of the experiment. Overlap of curves for each color was determined by using a histogram intersection method to find the minimum value between curves at any given decimal code point shown as:

$$\text{Overlap between Curves} = \frac{\sum \min|\text{trial at day}(x), \text{trial at time 0}(x)|}{\sum \text{trial at time 0}(x)}$$

Where x represents each pixel count value at every decimal code for each curve (Swain & Ballard, 1992). The minimum absolute value from each decimal code is taken and then summed to generate the total overlap which is then divided by total pixel counts to normalize the density of the curve to 1. To find the difference between the curves, which can be easier to interpret, used the equation:

$$\text{Difference between Curves} = 1 - \text{Overlap}$$

Where 1 represents the total density of all pixels in an image. The results of intersection analysis (Figure 15) for each day shows the fraction of pixels from each treated trial that share a minimum value with their control at the same decimal code. Low intersection values in overlap comparison express less similarity between color densities. A clear separation between treated trials (2, 3, and 4) and the control, trial 1, indicates clear identification of Cu contamination.

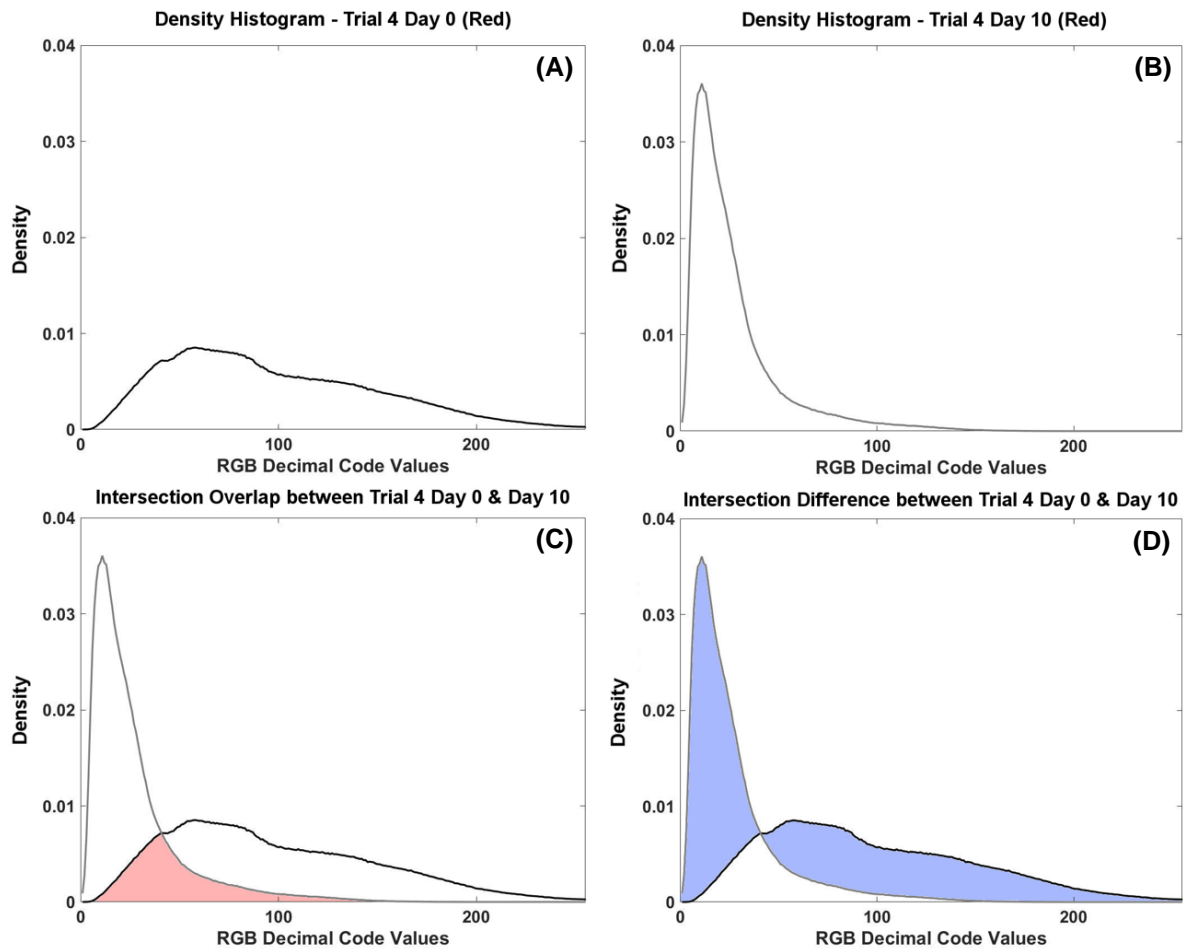


Figure 14: (A) Density histogram for Trial 4 day-0 red channel only. (B) Density histogram for Trial 4 day-10 red channel only. C and D plot density histograms A and B together and shows either the area of overlap (C) or the area of difference (D) based on the intersection method used to compare both curves.

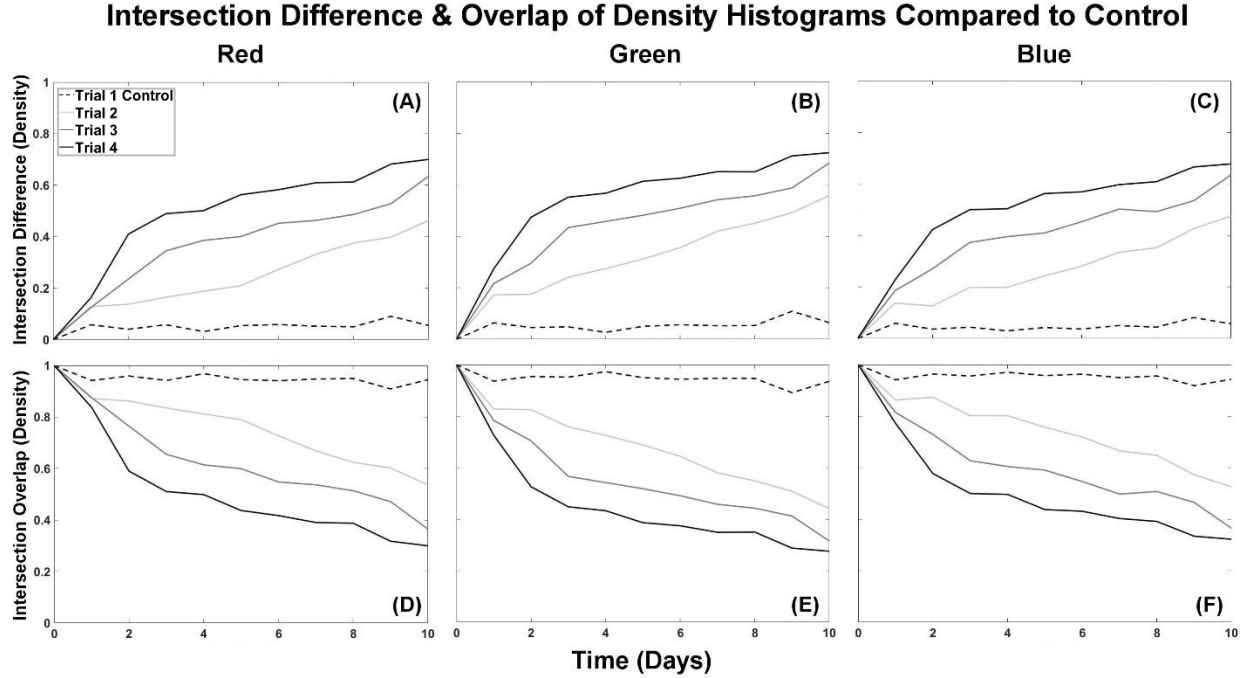


Figure 15: Intersection analysis with curve differences for R, G, and B (A-C) on top and curve overlap for R, G, and B (D-F) on the bottom. The control (dashed line) remains within a narrow range while treated trials continue to show more difference or less overlap with increased Cu toxicity. Each color channel appears to have similar behavior.

3.2.3. Single color pattern analysis

Color histogram overlaps and differences for R, G, and B appear similar (Figure 15) so only one color (red seemed most appropriate for the comparison to the other methods) was used for the following analysis. Intersection difference for red color for each trial on each day was plotted against their corresponding cumulative Cu dose (Table 2; Figure 16). In addition, the mean and standard deviation of trial 1 control were calculated at 95% (2σ) and 99.7% (3σ) confidence intervals. Standard deviation is calculated from the equation:

$$s = \sqrt{\frac{1}{n-1} \sum_{i=1}^n (x_i - \bar{x})^2}$$

Where s is the sample standard deviation, n is the number of samples in an individual trial ($n=11$), x_i each individual sample value, and \bar{x} is the mean of the trial (Wessel, 2018). Standard deviations for trial 1 from 10 days and point values of density differences for each treatment for each day are shown in Table 3. With no error assignable to these point values, Figure 16 and Table 3 reveal that all values for treated trials are outside of the trial 1 mean $\pm 3\sigma$ deviation interval.

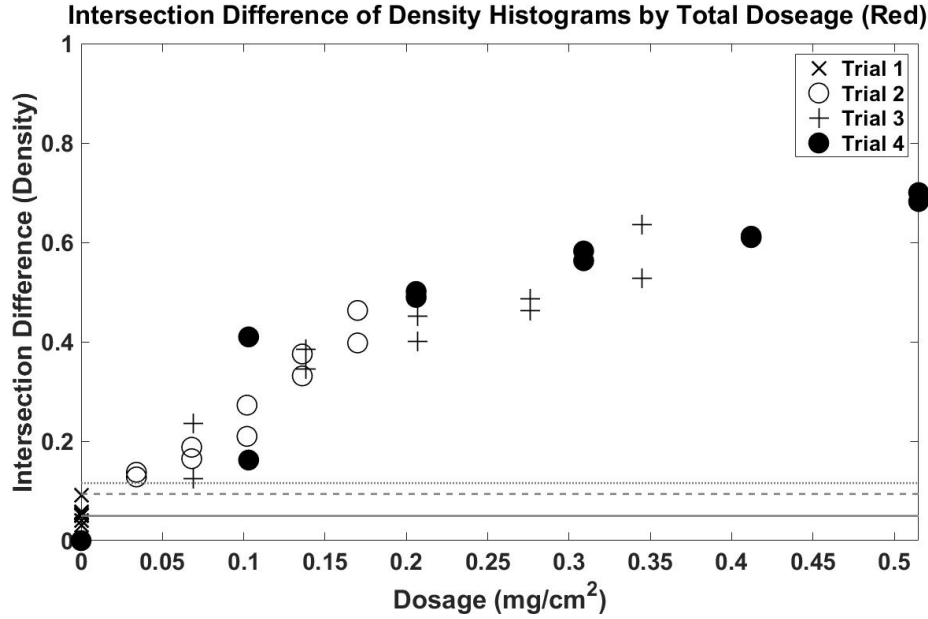


Figure 16: Plots of red color density differences for each trial on each day of the experiment relative to their day-0 control plotted against the cumulative Cu dose. 2 σ (dashed line) and 3 σ (dotted line) confidence intervals offset from the mean of trial 1 control.

Table 3. Standard deviation for histogram density differences for the red channel (Figure 15). Standard deviation and mean+stdev were calculated from the control at all 3 σ levels. Density difference values were calculated from $1 - \text{Histogram Overlap}$ (section 3.2.2) between treated trials and the day-0 control for each day to be compared with the confidence interval.

STDEV Trial 1	Base	Mean+STDEV	Trial	1	2	3	4	5	6	7	8	9	10
68%	.022	.072	2	.128	.137	.165	.188	.210	.273	.331	.375	.398	.463
95%	.044	.094	3	.124	.235	.345	.386	.401	.452	.463	.486	.528	.635
99%	.066	.116	4	.162	.410	.489	.501	.563	.583	.610	.612	.682	.700

Normalization plots on Figures B-1 and B-2 and corresponding discussion illustrated that color histograms change with added Cu dose. Another way to quantitatively express this difference is to look at the shapes or R, G, B histograms of pixel counts using the Dynamic Time Warping (DTW) and Curve Length (CL) methods (Jekel et al, 2018). Both are curve fitting techniques developed to look for differences between data sets without a need to fit a function or model through the data. Figure 16 shows the outcome of the DTW and CL analysis results plotted separately for each color in each trial, while Table 4 and 5 display the results of analysis. DTW expresses a difference between day-0 and day x (x=1 to 10) within each trial as a minimum cumulative distance between points on two curves. The CL method expresses the difference between two curves by comparing points along the x-axis by their individual ratios respective of the length of the overall curve. The control (trial 1) distance values remain relatively constant in all color channels for all days, while each of the treated trials shows a steady departure from their respective day-0 controls suggesting that there are differences in the R, G, and B colors between images taken at different stages and levels of doses in the experiment.

Table 4. Dynamic Time Warping non-linear (elastic) alignment distance results for all trial histograms delineated by color channel using day-0 control images specific to each trial. The table heading denotes the day of treatment that was compared to the day 0 control for each individual trial. The side of the table denotes trial number as detailed in Table 2, and the color delineation (white, light gray, and medium gray) represents the color channel that the data was generated for (red, green, and blue in order top to bottom).

	Trial	1	2	3	4	5	6	7	8	9	10	Mean
Red	1	1.04x10 ⁵	4.17x10 ⁴	3.64x10 ⁵	3.61x10 ⁴	6.14x10 ⁴	7.17x10 ⁴	5.15x10 ⁴	5.12x10 ⁴	2.47x10 ⁵	4.54x10 ⁴	1.07x10 ⁵
	2	8.06x10 ⁵	6.25x10 ⁵	1.04x10 ⁶	1.18x10 ⁶	1.32x10 ⁶	1.71x10 ⁶	2.08x10 ⁶	2.36x10 ⁶	2.50x10 ⁶	2.91x10 ⁶	1.65x10 ⁶
	3	7.83x10 ⁵	1.48x10 ⁶	2.17x10 ⁶	2.43x10 ⁶	2.52x10 ⁶	2.84x10 ⁶	2.91x10 ⁶	3.06x10 ⁶	3.32x10 ⁶	4.00x10 ⁶	2.55x10 ⁶
	4	1.02x10 ⁶	2.58x10 ⁶	3.08x10 ⁶	3.15x10 ⁶	3.54x10 ⁶	3.67x10 ⁶	3.84x10 ⁶	3.85x10 ⁶	4.29x10 ⁶	4.41x10 ⁶	3.34x10 ⁶
Green	1	1.07x10 ⁵	1.18x10 ⁵	3.02x10 ⁵	4.07x10 ⁴	4.40x10 ⁴	4.32x10 ⁴	3.36x10 ⁴	4.04x10 ⁴	6.83x10 ⁵	4.60x10 ⁴	1.46x10 ⁵
	2	9.60x10 ⁵	7.72x10 ⁵	1.51x10 ⁶	1.72x10 ⁶	1.96x10 ⁶	2.24x10 ⁶	2.64x10 ⁶	2.84x10 ⁶	3.09x10 ⁶	3.52x10 ⁶	2.13x10 ⁶
	3	1.36x10 ⁶	1.86x10 ⁶	2.73x10 ⁶	2.88x10 ⁶	3.03x10 ⁶	3.20x10 ⁶	3.41x10 ⁶	3.50x10 ⁶	3.70x10 ⁶	4.31x10 ⁶	3.00x10 ⁶
	4	1.72x10 ⁶	2.98x10 ⁶	3.47x10 ⁶	3.57x10 ⁶	3.86x10 ⁶	3.94x10 ⁶	4.10x10 ⁶	4.09x10 ⁶	4.48x10 ⁶	4.56x10 ⁶	3.68x10 ⁶
Blue	1	7.67x10 ⁴	2.27x10 ⁵	2.74x10 ⁵	1.84x10 ⁵	2.65x10 ⁵	3.36x10 ⁵	3.14x10 ⁵	2.74x10 ⁵	5.09x10 ⁵	5.75x10 ⁴	2.21x10 ⁵
	2	8.62x10 ⁵	7.93x10 ⁵	1.24x10 ⁶	1.24x10 ⁶	1.53x10 ⁶	1.77x10 ⁶	2.10x10 ⁶	2.21x10 ⁶	2.69x10 ⁶	2.99x10 ⁶	1.74x10 ⁶
	3	1.17x10 ⁶	1.70x10 ⁶	2.35x10 ⁶	2.49x10 ⁶	2.58x10 ⁶	2.85x10 ⁶	3.16x10 ⁶	3.10x10 ⁶	3.36x10 ⁶	4.00x10 ⁶	2.67x10 ⁶
	4	1.43x10 ⁶	2.66x10 ⁶	3.15x10 ⁶	3.17x10 ⁶	3.54x10 ⁶	3.58x10 ⁶	3.76x10 ⁶	3.83x10 ⁶	4.19x10 ⁶	4.26x10 ⁶	3.36x10 ⁶

Table 5. Curve Length Distance ratio results for all trial histograms delineated by color channel using day 0 control images specific to each trial. The table heading denotes the day of treatment that was compared to the day 0 control for each individual trial. The side of the table denotes trial number as detailed in Table 2, and the color delineation (white, light gray, and medium gray) represents the color channel that the data was generated for (red, green, and blue in order top to bottom).

	Trial	1	2	3	4	5	6	7	8	9	10	Mean
Red	1	6.70x10 ⁴	6.97x10 ⁴	7.40x10 ⁴	6.74x10 ⁴	7.58x10 ⁴	7.26x10 ⁴	7.28x10 ⁴	7.17x10 ⁴	6.19x10 ⁴	7.25x10 ⁴	9.31x10 ⁴
	2	6.28x10 ⁴	6.58x10 ⁴	6.43x10 ⁴	6.91x10 ⁴	6.80x10 ⁴	7.56x10 ⁴	8.27x10 ⁴	9.12x10 ⁴	9.48x10 ⁴	1.05x10 ⁵	1.09x10 ⁵
	3	6.33x10 ⁴	7.06x10 ⁴	8.44x10 ⁴	8.93x10 ⁴	9.64x10 ⁴	1.07x10 ⁵	1.06x10 ⁵	1.05x10 ⁵	1.16x10 ⁵	1.36x10 ⁵	1.46x10 ⁵
	4	7.23x10 ⁴	1.12x10 ⁵	1.24x10 ⁵	1.28x10 ⁵	1.46x10 ⁵	1.55x10 ⁵	1.61x10 ⁵	1.67x10 ⁵	1.99x10 ⁵	2.22x10 ⁵	1.96x10 ⁵
Green	1	8.05x10 ⁴	8.61x10 ⁴	9.37x10 ⁴	8.48x10 ⁴	9.09x10 ⁴	9.27x10 ⁴	8.68x10 ⁴	8.68x10 ⁴	7.60x10 ⁴	8.61x10 ⁴	8.66x10 ⁴
	2	8.49x10 ⁴	8.50x10 ⁴	9.15x10 ⁴	1.01x10 ⁵	1.04x10 ⁵	1.14x10 ⁵	1.23x10 ⁵	1.35x10 ⁵	1.43x10 ⁵	1.59x10 ⁵	1.10x10 ⁵
	3	9.34x10 ⁴	1.05x10 ⁵	1.29x10 ⁵	1.33x10 ⁵	1.49x10 ⁵	1.58x10 ⁵	1.62x10 ⁵	1.59x10 ⁵	1.94x10 ⁵	2.08x10 ⁵	1.42x10 ⁵
	4	1.11x10 ⁵	1.71x10 ⁵	1.98x10 ⁵	2.01x10 ⁵	2.31x10 ⁵	2.49x10 ⁵	2.47x10 ⁵	2.48x10 ⁵	2.73x10 ⁵	2.94x10 ⁵	2.09x10 ⁵
Blue	1	9.04x10 ⁴	9.10x10 ⁴	9.62x10 ⁴	9.42x10 ⁴	9.35x10 ⁴	9.97x10 ⁴	9.29x10 ⁴	9.18x10 ⁴	8.15x10 ⁴	9.34x10 ⁴	7.02x10 ⁴
	2	9.02x10 ⁴	8.92x10 ⁴	9.51x10 ⁴	1.04x10 ⁵	1.08x10 ⁵	1.13x10 ⁵	1.24x10 ⁵	1.36x10 ⁵	1.34x10 ⁵	1.34x10 ⁵	7.62x10 ⁴
	3	1.00x10 ⁵	1.15x10 ⁵	1.38x10 ⁵	1.38x10 ⁵	1.49x10 ⁵	1.62x10 ⁵	1.60x10 ⁵	1.72x10 ⁵	1.92x10 ⁵	2.02x10 ⁵	9.40x10 ⁴
	4	1.14x10 ⁵	1.62x10 ⁵	1.87x10 ⁵	1.92x10 ⁵	2.12x10 ⁵	2.29x10 ⁵	2.34x10 ⁵	2.28x10 ⁵	2.52x10 ⁵	2.64x10 ⁵	1.41x10 ⁵

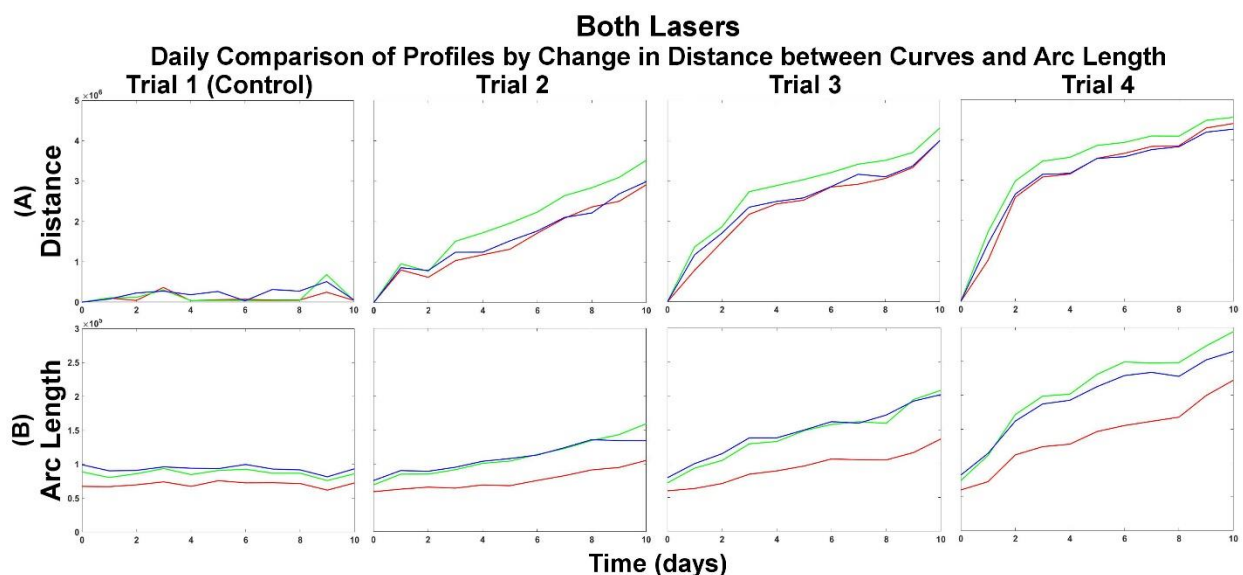


Figure 17: (A) The minimum cumulative difference in distance of R, G, and B curves between day 0 and consecutive day images as determined using DTW vs time for trial 1 control to trial 4. Each color channel is plotted for comparison. (B) The curve length method vs time measuring the curve length of each R, G, B curve. The curve lengths are plotted for each color in each trial for every day.

Standard deviations were also found for each color channel from DTW and CL values of trial 1 on days 1 through 10 ($n=10$) and compared to day-0 (Table 6). The disadvantage of this method is that trials 2, 3, and 4 DTW and CL values have no errors assigned. Though a 95% confidence interval is more than acceptable, looking at values exceeding 3σ of trial 1 mean standard deviation interval would be highly conclusive to decide which method produces more convincing evidence of distinguishing treated trials from the control. Comparing red channel DTW and CL distance between curve values (Tables 4 and 5) for each day in trials 2, 3, and 4 reveals that first day values of the treated trials for DTW in the red channel clear the trial 1 mean $\pm 3\sigma$ deviation interval. The same can be observed for the green blue channels for trial 3 and 4. However, trial 2 only clears 3σ deviation interval on day 3 (Cu dose of 3.16 mmol/cm^2 , equal to trial 3 day 1). Clear separation from the control trial may support the use of the red channel by itself as sufficient for contamination detection using LIF. Though, the lowest dose on day 2 from trial 2 (6.25×10^5) is within the trial 1 mean $\pm 3\sigma$ deviation interval, it is well above the 2σ 95% confidence level of 4.34×10^5 , within an acceptable level of statistical certainty.

For CL, results of standard deviation are far less conclusive. Looking again at the red channel it becomes apparent that no values are elevated above 3σ . Some samples at later days for trial 4 do clear the 99.7% level in the green channel, but the blue color channels behave the same as the red. Trial 4 only rises above the 1σ deviation interval (68%) on day 2, trial 3 by day 3, and trial 2 by day 6. It could be surmised that the normalization within the curve length method has brought all of the values too close together to use standard deviation effectively. Instead of just comparing their measurable difference to the control, all samples have been normalized to the control and then compared. The similarity between normalized plots from the qualitative analysis was one reason they were not used for quantitative comparison. Another possibility is

that CL is similar to using a Euclidean Distance measurement and may signal that one-dimensional analysis is not dynamic enough to describe the profiles generate from LIF. Compared to the DTW results, which could work for even lower levels of toxicity than 0.034 mg/cm², CL appears to be less useful.

Table 6. Standard Deviations (3σ) and Mean+STDEV of Trial 1 days 1 through 10 (n=10) compared to day-0 using DTW Histograms (each color), and Curve Length Histograms (each color). A min and max value from the red channel is also listed for quick comparison of the range of values for each method.

STDEV ONLY	DTW				Curve Length			
STDEV	Red	Green	Blue		Red	Green	Blue	
68%	1.10x10 ⁵	2.06x10 ⁵	1.43x10 ⁵		4.01x10 ³	5.14x10 ³	4.92x10 ³	
95%	2.19x10 ⁵	4.11x10 ⁵	2.85x10 ⁵		8.02x10 ³	1.03x10 ⁴	9.84x10 ³	
99.70%	3.29x10 ⁵	6.17x10 ⁵	4.28x10 ⁵		1.20x10 ⁴	1.54x10 ⁴	1.48x10 ⁴	
Mean+STDEV	DTW				Curve Length			
STD	Red	Green	Blue	Min Red	Red	Green	Blue	Min Red
68%	2.17x10 ⁵	3.51x10 ⁵	3.64x10 ⁵	6.25x10 ⁵	7.43x10 ⁴	9.18x10 ⁴	9.80x10 ⁴	6.28x10 ⁴
95%	4.34x10 ⁵	7.03x10 ⁵	7.28x10 ⁵	Max Red	1.49x10 ⁵	1.84x10 ⁵	1.96x10 ⁵	Max Red
99.70%	6.51x10 ⁵	1.05x10 ⁶	1.09x10 ⁶	4.41x10 ⁶	2.23x10 ⁵	2.75x10 ⁵	2.94x10 ⁵	2.22x10 ⁵

Another way of statistical comparison of trials is to use a t-Test (Wessel, 2018). However, while trial 1 mean and standard deviation is derived from 10 days (n=10), trials 2, 3, and 4 only have treatment cycles (when dose applied is the same) for 2 days (n=2) and that results in very low sample sizes. It was decided that a “master control” of all 10 days from trial 1 could be compared to each treated trial through a 3-point digital filtering interval technique (running average). To compare groups of different sizes, the Welch t-test was employed (Wessel, 2018). If the t-statistic is greater than t-critical (tcrit) then there is statistically significant difference between the points being compared. The Welch t-Test was performed for density histogram differences (Table 7), DTW in each color channel for histograms (Table 8), and for CL in each color channel for histograms (Table 9).

Results show that a difference between treated and control trials at 95% confidence interval can be proven for several methods. The density histogram differences pass at the 95% level save those comparisons that include a day-0 control. For DTW, all points pass the 95% level and only day 1 fails for all trials in all colors at the 99% confidence interval. CL is less useful, failing for trial 2, but still conclusive and in good agreement for trials 3 and 4. The 95% confidence interval for all methods is useful for delineating days and trials. Producing more images from each trial could help make the t-test more robust by increasing n and the results more conclusive towards identifying Cu toxicity. To evaluate the effectiveness of DTW for the red channel, it was plotted relative to dosage in Figure 18 to compare directly to density histogram differences (from Figure 16). Immediately the two trends appear the same, save DTW appears to have slightly more separation from 3σ . Such good agreement both statistically, through standard deviation and t-test, and visually by plotting of data by dosage may validate DTW as a viable method when compared to the more straight forward intersection density histograms.

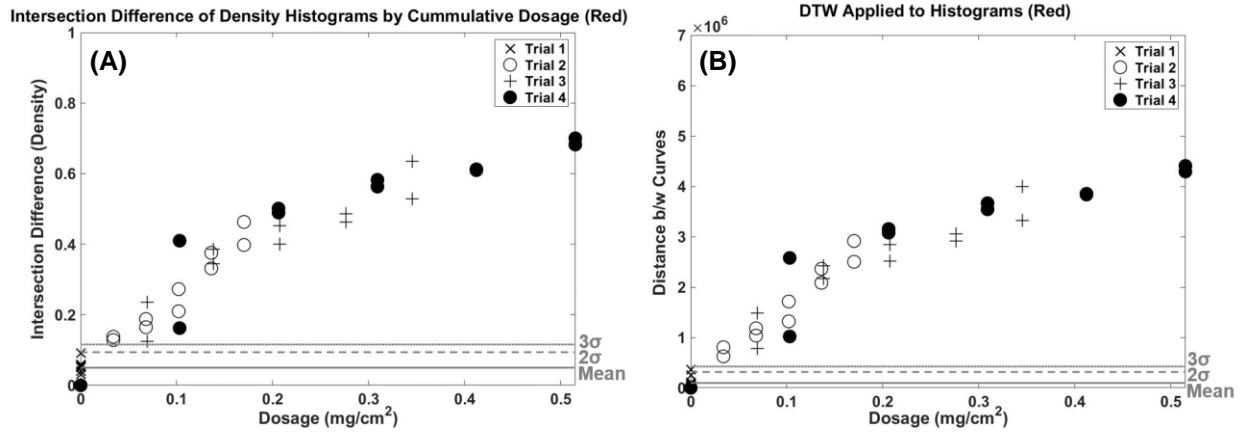


Figure 18: Red color density differences (A) and DTW (B) for each trial on each day of the experiment relative to their day-0 control plotted against the cumulative Cu dose. 2 σ (dashed line) and 3 σ (dotted line) confidence intervals offset from the mean of trial 1 control.

Table 7. Density Histogram difference result for the red channel from the Welch t-test for confidence intervals at 2σ (95%) and 3σ (99%). Trials represent a running average of 3 data points to remove aliasing and increase the overall degrees of freedom. Treatment level for the middle point of the 3-point average is included to compare thresholds that pass with a statistical certainty.

Trial	95%	99%	t	mg/cm²
2.0-2	2.835	6.571	-0.863	0.034
2.1-3	2.198	3.975	-7.291	0.034
2.2-4	2.390	4.682	-7.101	0.068
2.3-5	2.313	4.388	-9.443	0.068
2.4-6	2.690	5.914	-6.615	0.102
2.5-7	2.790	6.361	-6.196	0.102
2.6-8	2.746	6.160	-9.061	0.136
2.7-9	2.568	5.393	-15.459	0.136
2.8-10	2.703	5.972	-13.362	0.170
3.0-2	2.883	6.790	-1.027	0.069
3.1-3	2.878	6.766	-2.894	0.069
3.2-4	2.838	6.579	-5.996	0.138
3.3-5	2.477	5.024	-18.240	0.138
3.4-6	2.585	5.466	-17.107	0.207
3.5-7	2.562	5.369	-19.057	0.207
3.6-8	2.134	3.757	-34.747	0.276
3.7-9	2.557	5.350	-21.867	0.276
3.8-10	2.836	6.571	-11.153	0.345
4.0-2	2.908	6.907	-1.180	0.103
4.1-3	2.902	6.880	-3.078	0.103
4.2-4	2.734	6.106	-14.163	0.206
4.3-5	2.646	5.723	-19.674	0.206
4.4-6	2.676	5.854	-19.645	0.309
4.5-7	2.339	4.487	-35.615	0.309
4.6-8	2.100	3.637	-47.706	0.412
4.7-9	2.663	5.797	-23.707	0.412
4.8-10	2.710	6.002	-22.285	0.515

Table 8. DTW result for all color channels from the Welch t-test for confidence intervals at 2σ (95%) and 3σ (99%). Trials represent a running average of 3 data points to remove aliasing and increase the overall degrees of freedom. Treatment level for the middle point of the 3-point average is included to compare thresholds that pass with a statistical certainty.

Trials	DTW RED			DTW GREEN			DTW BLUE			mg/cm ²
	95%	99%	t	95%	99%	t	95%	99%	t	
1v2.1-3	2.648	5.732	-5.729	2.640	5.698	-4.051	2.592	5.493	-5.090	0.034
1v2.2-4	2.765	6.247	-4.940	2.740	6.136	-4.031	2.626	5.639	-5.585	0.068
1v2.3-5	2.430	4.836	-12.195	2.327	4.443	-10.898	2.375	4.622	-10.454	0.068
1v2.4-6	2.751	6.183	-7.984	2.424	4.813	-11.162	2.639	5.694	-8.088	0.102
1v2.5-7	2.827	6.527	-7.184	2.584	5.461	-10.272	2.672	5.835	-9.216	0.102
1v2.6-8	2.796	6.386	-10.149	2.523	5.207	-12.913	2.566	5.385	-12.923	0.136
1v2.7-9	2.660	5.784	-17.201	2.328	4.447	-18.629	2.708	5.991	-11.313	0.136
1v2.8-10	2.762	6.235	-14.722	2.587	5.475	-14.377	2.778	6.304	-10.400	0.170
1v3.1-3	2.891	6.826	-3.410	2.822	6.504	-4.531	2.853	6.651	-4.412	0.069
1v3.2-4	2.863	6.694	-6.721	2.770	6.268	-7.223	2.794	6.380	-7.912	0.138
1v3.3-5	2.583	5.455	-20.503	2.058	3.501	-25.244	2.125	3.723	-27.902	0.138
1v3.4-6	2.663	5.798	-19.274	2.098	3.632	-25.576	2.448	4.907	-20.636	0.207
1v3.5-7	2.648	5.731	-21.202	2.212	4.023	-24.020	2.678	5.860	-15.224	0.207
1v3.6-8	2.282	4.276	-38.452	2.073	3.552	-29.273	2.362	4.575	-26.785	0.276
1v3.7-9	2.647	5.726	-23.974	2.051	3.481	-31.516	2.233	4.098	-32.939	0.276
1v3.8-10	2.861	6.688	-11.873	2.681	5.875	-14.638	2.814	6.472	-12.040	0.345
1v4.1-3	2.908	6.906	-3.411	2.860	6.684	-4.907	2.890	6.821	-4.268	0.103
1v4.2-4	2.784	6.335	-15.478	2.541	5.284	-16.503	6.821	5.852	-16.044	0.206
1v4.3-5	2.717	6.034	-21.388	2.255	4.176	-26.060	2.543	5.290	-22.775	0.206
1v4.4-6	2.746	6.163	-20.906	2.227	4.078	-28.061	2.559	5.356	-23.235	0.309
1v4.5-7	2.475	5.015	-38.234	1.949	3.161	-39.815	2.132	3.748	-41.872	0.309
1v4.6-8	2.210	4.016	-54.165	1.844	2.852	-46.889	2.196	3.967	-40.221	0.412
1v4.7-9	2.730	6.089	-25.505	2.319	4.411	-28.334	2.570	5.402	-26.345	0.412
1v4.8-10	2.771	6.273	-23.462	2.402	4.726	-26.594	2.570	2.570	-27.530	0.515

Table 9. CL result for all color channels from the Welch t-test for confidence intervals at 2 σ (95%) and 3 σ (99%). Trials represent a running average of 3 data points to remove aliasing and increase the overall degrees of freedom. Treatment level for the middle point of the 3-point average is included to compare thresholds that pass with a statistical certainty.

Trial	Curve RED			Curve GREEN			Curve BLUE			mg/cm ²
	95%	99%	t	95%	99%	t	95%	99%	t	
1v2.1-3	1.814	2.767	3.996	2.038	3.437	-0.251	2.011	3.353	0.408	0.034
1v2.2-4	1.952	3.169	2.153	2.528	5.229	-1.225	2.560	5.359	-0.800	0.068
1v2.3-5	1.963	3.203	1.749	2.398	4.712	-2.999	2.490	5.076	-2.421	0.068
1v2.4-6	2.265	4.213	-0.133	2.426	4.820	-4.647	2.237	4.113	-5.296	0.102
1v2.5-7	2.621	5.617	-1.102	2.616	5.596	-4.740	2.608	5.563	-4.550	0.102
1v2.6-8	2.649	5.736	-2.691	2.663	5.796	-5.948	2.744	6.153	-4.683	0.136
1v2.7-9	2.533	5.249	-4.987	2.643	5.710	-7.800	2.474	5.010	-9.723	0.136
1v2.8-10	2.608	5.562	-6.108	2.720	6.046	-8.162	1.796	2.719	-25.926	0.170
1v3.1-3	2.763	6.236	-0.352	2.822	6.507	-2.137	2.851	6.642	-2.261	0.069
1v3.2-4	2.732	6.100	-1.895	2.783	6.330	-4.030	2.784	6.332	-4.850	0.138
1v3.3-5	2.516	5.180	-5.243	2.665	5.804	-7.973	2.466	4.980	-12.438	0.138
1v3.4-6	2.702	5.968	-5.095	2.732	6.099	-8.025	2.757	6.211	-8.065	0.207
1v3.5-7	2.498	5.107	-9.003	2.411	4.764	-16.633	2.525	5.215	-14.989	0.207
1v3.6-8	1.796	2.719	-24.941	1.822	2.790	-35.211	2.474	5.010	-18.061	0.276
1v3.7-9	2.521	5.199	-10.271	2.834	6.560	-7.524	2.825	6.522	-8.698	0.276
1v3.8-10	2.842	6.601	-5.287	2.868	6.718	-6.855	2.815	6.473	-10.757	0.345
1v4.1-3	2.893	6.836	-2.056	2.903	6.883	-2.855	2.901	6.875	-2.882	0.103
1v4.2-4	2.676	5.854	-10.200	2.804	6.422	-10.688	2.824	6.517	-9.351	0.206
1v4.3-5	2.786	6.342	-9.018	2.823	6.512	-11.579	2.783	6.328	-13.436	0.206
1v4.4-6	2.820	6.498	-9.009	2.864	6.699	-9.967	2.847	6.621	-10.981	0.309
1v4.5-7	2.633	5.670	-18.349	2.634	5.671	-26.229	2.745	6.156	-19.428	0.309
1v4.6-8	2.513	5.167	-24.450	1.803	2.737	-90.120	2.021	3.384	-58.002	0.412
1v4.7-9	2.873	6.743	-8.860	2.776	6.298	-19.551	2.768	6.260	-19.768	0.412
1v4.8-10	2.894	6.841	-7.841	2.858	6.672	-13.819	2.845	6.614	-14.555	0.515

3.2.4. Two color pattern analysis

All the above analyses quantified differences between individual colors over time and did not take advantage of the composite information provided by the combination of colors in the images. The stacked red versus green plots (Figures 8-11) use the combination of two colors and show a visual separation between the control and various treatment levels in the shapes and the lengths of the “loops”. One way to quantify this difference is to identify the furthest point of the loop (apex) from the origin (Figure 19) that were produced using the density histogram differences. The apex is defined by the peaks of the R and G densities, and while this approach is not ideal because its one-dimensionality ignores the shape of the loop (e.g. its area, width), it allows for a mathematical expression of the differences between the “loops” (Table 10). To check the method, a standard deviation and mean were found for the trial 1 control at 2σ and 3σ confidence interval (Figure 18). Trial 2 clearly separates from the control by day six and trials 3 and 4 by days 1 and 2, respectively as visually observed in the red versus green plots.

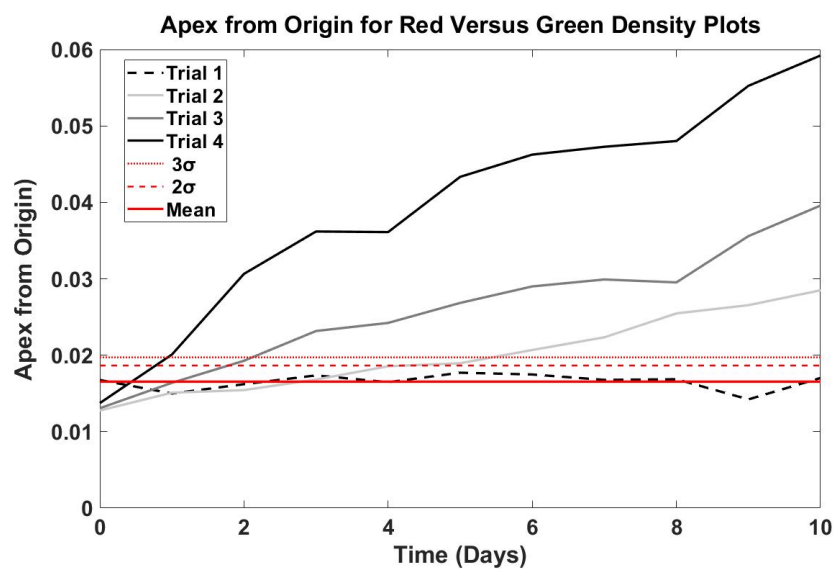


Figure 19: Plots of apex from origin from red versus green density difference plots for each trial on each day of the experiment. 2σ confidence interval (dashed line) and 3σ confidence interval (dotted line) offset from the mean of the control (solid line).

Table 10. Loop distance from origin results for all days for all trials red versus green plots using day-0 control images specific to each trial.

Day	1	2	3	4	5	6	7	8	9	10
1	4.72×10^4	5.10×10^4	5.46×10^4	5.18×10^4	5.57×10^4	5.50×10^4	5.28×10^4	5.30×10^4	4.47×10^4	5.35×10^4
2	4.75×10^4	4.86×10^4	5.29×10^4	5.84×10^4	5.96×10^4	6.51×10^4	7.03×10^4	8.01×10^4	8.35×10^4	8.96×10^4
3	5.16×10^4	6.06×10^4	7.29×10^4	7.62×10^4	8.44×10^4	9.12×10^4	9.41×10^4	9.29×10^4	1.12×10^5	1.25×10^5
4	6.32×10^4	9.64×10^4	1.14×10^5	1.14×10^5	1.36×10^5	1.45×10^5	1.49×10^5	1.51×10^5	1.74×10^5	1.86×10^5

DTW was also applied to the red versus green plots (Figure 20) as it can be applied to determine differences in geometric shapes delineated by single curves. This analysis has the advantage over the Apex distance from origin approach in that it accounts for the whole shape of the loops. For this analysis pixel counts were used instead of densities. Results from DTW for red versus green plots are shown in Table 11. CL methods struggled to accurately process the “loops,” because it compares ratios and has a normalizing step, the irregular shapes become too difficult to compare and processing results in non-values.

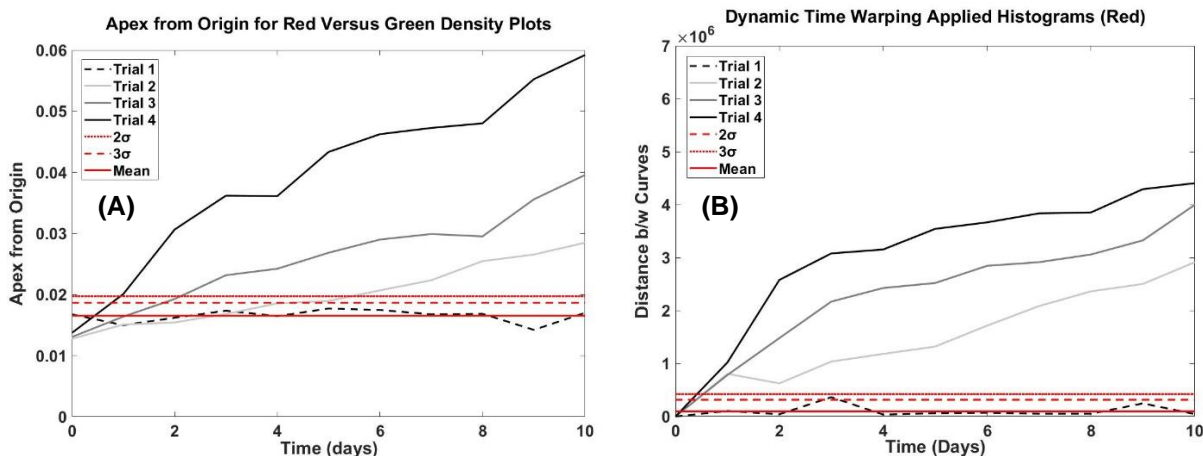


Figure 20: (A) Plot of Apex from origin from red versus green loops using density differences for each trial on each day of the experiment. (B) DTW plot of non-linear alignment distance between red vs green loops from full image pixel counts for day-0 and consecutive days of each trial vs time.

Table 11. Distance Time Warping non-linear (elastic) alignment distance results for all trial red versus green plots using before treatment control images specific to each trial

	1	2	3	4	5	6	7	8	9	10
1	2.71x10 ⁵	2.48x10 ⁵	5.15x10 ⁵	1.59x10 ⁵	2.06x10 ⁵	3.23x10 ⁵	2.54x10 ⁵	2.76x10 ⁵	6.01x10 ⁵	2.76x10 ⁵
2	1.46x10 ⁶	1.11x10 ⁶	1.97x10 ⁶	2.26x10 ⁶	2.54x10 ⁶	3.02x10 ⁶	3.59x10 ⁶	3.95x10 ⁶	4.27x10 ⁶	4.87x10 ⁶
3	1.71x10 ⁶	2.56x10 ⁶	3.71x10 ⁶	4.01x10 ⁶	4.17x10 ⁶	4.55x10 ⁶	4.75x10 ⁶	4.90x10 ⁶	5.25x10 ⁶	6.17x10 ⁶
4	2.19x10 ⁶	4.20x10 ⁶	4.90x10 ⁶	5.04x10 ⁶	5.51x10 ⁶	5.65x10 ⁶	5.87x10 ⁶	5.87x10 ⁶	6.44x10 ⁶	6.57x10 ⁶

Standard deviation for trial 1 for Apex and DTW for red versus green plots were also calculated (Table 12) as well as Welch t-tests (Table 13) analogously to the approach described in single color analysis. Comparison of treated trials to the mean ± σ standard deviation of control using Apex from origin is similar to CL in that it fails for trial 2 at the early doses of the experiment even at the 95% confidence interval. DTW for red versus green passes at all 95% interval levels making it in good agreement with DTW for individual colors and with density histogram difference values. Combined red versus green DTW could increase the sensitivity of the measurement allowing for greater confidence in determining successful detection. As such, DTW for red versus green plots was plotted relative to cumulative Cu dosage (Figure 21) and

compared to DTW for just the red channel (from Figure 18). The trend is similar here with a slight exaggeration as the points become more separated when using two-color analysis versus single color. There is greater separation from 3σ and better delineation between individual points that share the same dosage cycle (48-hours).

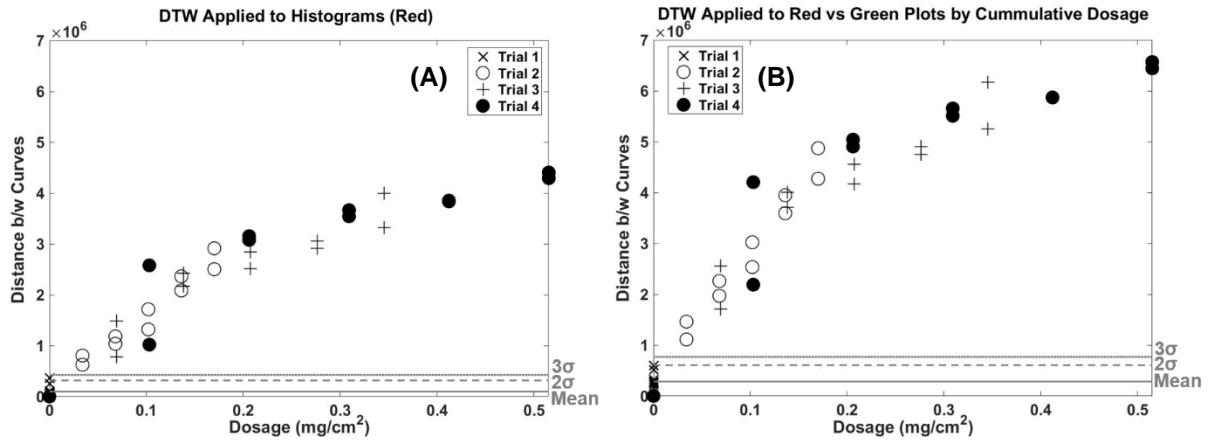


Figure 21: Red color DTW (A) and red versus green DTW (B) for each trial on each day of the experiment relative to their day-0 control plotted against the cumulative Cu dose. 2σ (dashed line) and 3σ (dotted line) confidence intervals offset from the mean of trial 1 control.

Table 12. Standard Deviations of trial 1 means to 3 σ for Apex distance from origin, and DTW for red versus green plots. Values are taken from full pixel counts and not densities.

STDEV ONLY	Apex		R vs G	
68%	3.51x10 ³		1.38x10 ⁵	
95%	7.01x10 ³		2.76x10 ⁵	
99.70%	1.05x10 ⁴		4.14x10 ⁵	
Mean+STDEV	Apex	Min	R vs G	Min
68%	5.54x10 ⁴	4.75x10 ⁴	4.51x10 ⁵	1.11x10 ⁶
95%	5.89x10 ⁴	Max	9.01x10 ⁵	Max
99.70%	6.25x10 ⁴	1.86x10 ⁵	1.35x10 ⁶	6.57x10 ⁶

Table 13. Apex and DTW for red versus green plots result from the Welch t-test for confidence intervals at 2 σ (95%) and 3 σ (99%). Trials represent a running average of 3 data points to remove aliasing and increase the overall degrees of freedom. Treatment level is included for the mid-point to compare thresholds that pass with a statistical certainty.

Treatment	Apex			DTW R vs G			mg/cm ²
	95%	99%	t	95%	99%	t	
1v2.1-3	2.126	3.727	1.140	2.807	6.439	-4.736	0.034
1v2.2-4	2.488	5.067	-0.450	2.859	6.677	-4.215	0.068
1v2.3-5	2.278	4.261	-2.151	2.684	5.888	-11.418	0.068
1v2.4-6	2.278	4.261	-3.887	2.780	6.316	-10.142	0.102
1v2.5-7	2.538	5.270	-3.982	2.842	6.598	-8.927	0.102
1v2.6-8	2.703	5.972	-4.389	2.823	6.512	-11.695	0.136
1v2.7-9	2.661	5.788	-6.336	2.746	6.162	-18.011	0.136
1v2.8-10	2.476	5.017	-10.852	2.822	6.508	-14.828	0.170
1v3.1-3	2.801	6.412	-1.558	2.898	6.859	-4.039	0.069
1v3.2-4	2.730	6.090	-3.687	2.882	6.786	-7.012	0.138
1v3.3-5	2.592	5.496	-7.207	2.594	5.502	-25.761	0.138
1v3.4-6	2.698	5.949	-7.150	2.673	5.840	-23.681	0.207
1v3.5-7	2.496	5.100	-12.324	2.697	5.944	-23.787	0.207
1v3.6-8	1.834	2.823	-29.315	2.428	4.829	-40.053	0.276
1v3.7-9	2.802	6.413	-7.607	2.639	5.694	-30.136	0.276
1v3.8-10	2.866	6.708	-6.182	2.869	6.724	-13.449	0.345
1v4.1-3	2.898	6.861	-2.629	2.909	6.910	-4.242	0.103
1v4.2-4	2.790	6.359	-9.413	2.815	6.476	-16.702	0.206
1v4.3-5	2.834	6.562	-9.358	2.726	6.072	-25.517	0.206
1v4.4-6	2.864	6.702	-8.598	2.726	6.072	-26.835	0.309
1v4.5-7	2.648	5.734	-22.846	2.449	4.912	-47.262	0.309
1v4.6-8	2.171	3.881	-46.271	2.209	4.012	-64.270	0.412
1v4.7-9	2.847	6.624	-13.100	2.736	6.116	-29.481	0.412
1v4.8-10	2.875	6.752	-11.464	2.772	6.278	-27.265	0.515

3.2.4. 48-hour analysis

To better understand the dynamic shift in images in response to the applied Cu dose, the first 48-hours of the experiment were also analyzed. Images produced within 0, 6, 12, 24, 36 and 48-hours after the first applied Cu dose for all four trials were reexamined to explore changes within between dosing periods. Analysis of this interval will also reveal whether the assumption based on preliminary work showing no change in the moss 48-hours after Cu dosing remains true for the parameters of this experiment. The information gained from the control (trial 1), which did not receive a Cu dose, shows that images taken of the moss during day versus night, as well as before and after wetting at 24-hours fails to show significant difference. Trials with Cu doses showed a time lapse of moss response to an initial individual Cu dose. Only the red channel was used to create density intersection histogram differences (Figure 22a). These values were also used to plot each trial based on dosage for comparison to the trial 1 mean and 2σ and 3σ standard deviations (Figure 22b). Each of the treated trials show increase following treatment but begin to flatten over time. All trials clear the 95% confidence interval for all hours during the treatment cycle (Table 14). A Welch t-test was also conducted with a running average with values passing the 95% confidence interval save those averages including a day-0 control value.

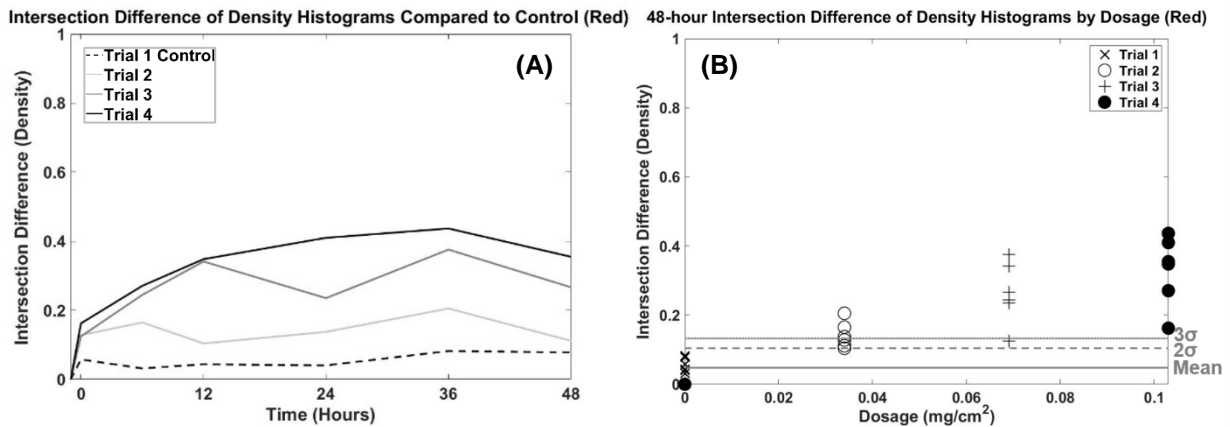


Figure 22: (A) Plot of intersection density difference by time in hours (A) and by dosage (B) for each trial over first 48-hours.

Table 14. Standard deviation for histogram density differences for the red channel (Figure 19). Standard deviation and mean+stdev were calculated from the control at all 3 σ levels. Density difference values are calculated from 1 – Histogram Overlap (section 3.2.2) between treated trials and the control for each day to be compared with the confidence interval.

STDEV	Base	Mean+	Trial	0	6	12	24	36	48
68%	0.028	0.076	2	0.128	0.165	0.104	0.137	0.205	0.112
95%	0.057	0.104	3	0.124	0.245	0.341	0.235	0.376	0.267
99%	0.085	0.133	4	0.162	0.271	0.348	0.410	0.437	0.355

Table 15. Density Histogram difference result for the red channel from the Welch t-test for confidence intervals at 2 σ (95%) and 3 σ (99%). Trials represent a running average of 3 data points to remove aliasing and increase the overall degrees of freedom. Treatment level for the middle point of the 3-point average is included to compare thresholds that pass with a statistical certainty.

Trial	95%	99%	t	hr	mg/cm ²
2.0-2	2.758	6.214	-0.979	0	0.034
2.1-3	2.210	4.015	-4.090	6	0.034
2.2-4	2.206	4.003	-4.258	12	0.034
2.3-5	2.540	5.278	-3.201	24	0.034
2.4-6	2.503	5.128	-3.472	36	0.034
3.0-2	2.916	6.947	-1.056	0	0.069
3.1-3	2.812	6.463	-2.973	6	0.069
3.2-4	2.608	5.562	-6.359	12	0.069
3.3-5	2.703	5.970	-6.187	24	0.069
3.4-6	2.705	5.982	-5.576	36	0.069
4.0-2	5.982	6.953	-1.217	0	0.103
4.1-3	2.778	6.307	-3.869	6	0.103
4.2-4	2.684	5.888	-7.089	12	0.103
4.3-5	2.467	4.983	-12.356	24	0.103
4.4-6	2.413	4.770	-13.379	36	0.103

4. Discussion

Qualitative and quantitative analysis of all color channels for trial 1 (control) images over the 10-day duration of the experiment showed very little variation in their color distribution (Figures 4-11 and 15-19). This suggests that the conditions and methods used for moss cultivation in the grow tent were appropriate and stable. In addition, the 0 to 48-hour observations of trial 1 further support that there is no discernable difference in moss response during day and night imaging or before and after wetting (Figure 22). In contrast, qualitative observations of treated moss concluded that a characteristic pattern emerged in response to Cu treatments by showing a shift in the modes of red and green color distributions towards lower, “darker” decimal codes (Figure 13). Higher Cu doses resulted in taller, more right skewed peaks in the density histograms while the control remained unchanged. Master histograms combining all color channels (Figure 12) and red versus green plots (Figures 8-11) make it easier to compare each treated trial directly to the control. For example, it is clear that trial 4, which receives an initial dose of $0.103\text{mg}/\text{cm}^2$, shows a clear separation from its day-0 control starting on day 1. The other trials have less obvious separation in the early days of the experiment.

Histograms and densities of individual colors extracted from images were quantitatively analyzed using histogram overlap and difference (Figures 15-16) as well as DTW and CL techniques (Figure 17; Tables 4-5). These methods allow differences between images taken before and after Cu treatment to be expressed as numerical values which are then analyzed by comparing their overlap or separation from the mean \pm standard deviation of the trial 1 control (no Cu treatment) and complemented by Welch’s t-test. These analyses show that images collected over 10 days of the experiment for all treated samples using density differences, DTW for color channel histograms, and DTW for red versus green plots differ from the trial 1 mean \pm standard deviation to 3σ (99.7%). This means that LIF is capable of differentiating Cu treated moss images from controls at Cu wet deposition levels from single doses at $0.034\text{ mg}/\text{cm}^2$ through cumulative doses of $0.515\text{ mg}/\text{cm}^2$ tested here, or potentially higher. Apex-distance and CL appear to be less sensitive methods than DTW which may be due to their one-dimensional analysis. Though there were lower quantified difference values for trial 2 and a higher mean \pm standard deviation for trial 1, all methods and trials differed at 2σ (95%).

It is of importance to note that multiple incremental doses and one individual dose result in the same final Cu level induced similar response (Figure 16). Trial 2 day 5 ($0.102\text{ mg}/\text{cm}^2$) falls near the day 1 value of trial 4 ($0.103\text{mg}/\text{cm}^2$). Trial 2 day 7-8 ($0.138\text{ mg}/\text{cm}^2$) can be seen to overlap with trial 3 day 3-4 ($0.136\text{ mg}/\text{cm}^2$). This is encouraging as it suggests that it may be possible to use LIF to quantify Cu doses the moss was exposed to. Density histogram differences and DTW seem to provide the same level of confidence, while CL is a less sensitive method for identifying deviation from the control. Methods that take advantage of the co-evolution of more than one color were also explored by plotting red against green pixel counts for corresponding decimal codes. The resulting shapes had a loop form and showed a gradual change in size and shape with increasing Cu dose (Figure 9 and 11). This shape change was successfully quantified using the DTW method when compared to the trial 1 mean \pm standard deviation at 2σ . Because all treatment levels produced a quantifiable difference from the control, it is not possible to derive a

threshold value for this method. We can only say that LIF is capable of identifying the lowest applied dose of Cu contamination at 0.034 mg/cm².

The lowest Cu value of 0.034 mg/cm² or 340 mg/m² is well above published environmental levels in wet deposition in urban environments, which range 0.49-2.2 mg/m²/yr in 5 cities in New Jersey (Reinfelder et al., 2005), 0.70 mg/m²/yr in suburban Reston, Virginia (Conco et al., 2004) and 1.06 mg/m²/yr in Chicago, Illinois (Colman et al., 2001) in the US. Similarly, a compilation of global studies by Pan and Wang (2015) report an average wet deposition of 0.8±0.7 mg/m²/yr in urban areas but also 4.7 mg/m²/yr for Hong Kong, China, 14.6 mg/m²/yr for Singapore, and 10.50 mg/m²/yr in the North Sea. Wet and dry deposition are the major sources of Cu for moss uptake. A study of mosses around Chengdu city in Southwest China showed Cu levels ranging from 19.5 ± 3.6-139 ± 27 µg/g (Chen et al., 2010). A survey of 178 sites across Portugal used *Hypnum cupressiforme* Hedw. and *Scleropodium touretii* (Brid.) L. Kock and found a 0.4-52.01 µg/g range of Cu (Figueira et al., 2002). In Portland, Oregon, 346 moss samples (*Orthotrichum lyellii* Hook. & Taylor) over 3 weeks showed a mean of 20 mg/kg, but a maximum value of 357.25 mg/kg (Gatziolis et al., 2016).

The high moss Cu level in Portland was attributed to glass manufacturing and industry. Heavy metal introduction into the environment from anthropogenic sources is predominantly from production or processing of metals in mining, smelting, waste incineration, and fossil fuel industries (Hoodaji et al., 2012). The key difference between the urban areas and long-term environmental effects from mining and industry appears to be that industrial sources result in significant dry deposition. Dry deposition in the form of particulates are carried through the atmosphere via wind and gravity to biota. However, the ratio of Cu that is soluble and available for uptake is variable and thus not directly comparable to wet deposition values. Nevertheless, dry deposition has been reported to have up to 0.5 mg/m²/d of Cu at an industrial site in Romania (Velea et al., 2009). Heavy metal deposition in Nigeria is linked to petroleum product depots with sampling of *Barbula lambarenensis* showing particulate accumulation in mosses ranging from 5.88-8.71 mg/kg at 4 sampling sites (Fatoba et al., 2013). Copper measurements of environmental samples show that in-situ concentrations of Cu in moss can be 1-10 times the local soil levels (Shacklette & Hansford, 1967). Moss (*Hylocomium splendens*) in Alaska was found to have 2.4-7.48 mg/kg (Brumbaugh et al., 2016), and historical levels of Cu in lichen (*Xanthoparmelia*) was 12.07-73.3 mg/kg in Arizona (Zschau et al., 2003). Yet, even expanded to an annual estimate, these are still below detection levels of LIF as presented here.

A look at more industrial areas, such as the thermoelectric Nikola Tesla power plant in Serbia, begins to show scenarios where levels are 100x above urban areas and may be closer to those currently detectable using LIF. Moss sampling revealed a range of 14.27-37.23 mg/kg around Nikola Tesla plant compared to thermal power plants in Canada which show an average 19.8 mg/kg sampling (Ćujić et al, 2013). Such high values were attributed to poor quality lignite excavation sites and local wind patterns. The Murgul copper mine in Turkey showed a 9-13 mg/kg/day value in dry deposition, but comparison of 23 different sites and 13 moss species revealed values ranging from 105-1916mg/kg. Even the control samples collected over 1 month had a higher than environmental level of Cu and ranged from 105-147 mg/kg. Soil samples in the area showed ranges of 81-1266 mg/kg (Koz et al., 2012). Wahsha et al. (2012) assessed metal toxicity in soils and their accumulation in plants in Northeast Italy. Soil samples could reach 20-

3975 mg/kg over 17 sampling sites even though industrial limits are set to 600 mg/kg. Cu accumulation in plants by comparison is much lower than these values, at 16-81 mg/kg in the common dandelion (*Taraxacum officinale* Weber ex F.H.Wigg. 1780) and different willows (*Salix purpurea* L., *Salix caprea* L., and *Salix elaeagnos* Scop.), but still very high when considering a yearly dose (Wahsha et al., 2012).

Though the LIF method for Cu range tested here has minimal application outside of extreme cases, the lowest threshold determined is only a magnitude or 2 higher than levels found in the literature. Adjustment of laser intensity or gain could increase sensitivity for detection. In terms of the success of the laser in detecting Cu, the density difference and DTW methods for single-color histograms and red vs green plots are in good agreement and show potential for in-situ applications where a set of moss images would be collected and evaluated against an uncontaminated control. However, in-situ applications of LIF imaging will encounter multiple further challenges, such as moss response to changes in growing conditions as opposed to our controlled experiment. Moss growth depends on many factors such as light, temperature, nutrient availability, and water content, which can each affect LIF and chlorophyll behavior (Yang-Er et al., 2019). Further, only singular images of each trial were collected, but future work should focus on collecting batches of images of moss samples to enable a more robust statistical analysis.

Further exploration of the relationship between red and green channels is of great interest. In all the treated trials, the red and green histograms shifted toward lower decimal codes with increasing Cu treatment and some higher (lighter) RGB decimal code values were eliminated entirely. It is hypothesized that this may be the result of chlorophyll dominance shifting from chl-a to chl-b or total chlorophyll reduction in response to metal toxicity (Tremper et al., 2004; Sun et al., 2009; Shakya et al., 2008). Experiments extracting chlorophyll content and measuring the levels of both chl-a and chl-b may help confirm that. Variation or reduction in the levels of chlorophyll a or b may be linked to changes in LIF image profiles but other processes like cellular death might also be involved (Yang-Er, 2019). The exact mechanism of moss fluorescence change is yet to be determined. Future work should also include observation of moss contaminated with different metals and organic contaminants.

5. Conclusion

The research detailed in this paper set out to design and implement a replicable methodology and prove the viability of using a new LIF technology (Biofinder, Misra et al., 2018) to detect copper contamination in moss. Images of fluorescence of moss subjected to Cu doses showed changes in red and green color distributions compared to controls. Density intersection histogram differences and DTW were successfully applied to single color analysis, and DTW was proved the dominant method when applied to red versus green plots extracted from images taken after different Cu doses. This quantitative analysis of images presented in this work prove that metal contamination of moss samples at a 0.034 mg/cm² level can be distinctly identified using the Biofinder with potential for a lower level of detection. Though this level of detection is higher than Cu reported in urban settings and background sources, it may be applicable to mining, industry, Superfund, or sewage sludge deposit sites. Future work will explore the lowest threshold for Cu identification using LIF and the possibility of quantification of Cu does the moss was exposed. In addition, effects of individually applied or a mixture of other metals of interest and organic pollutants will also be explored as well as LIF imaging of stress (temperature, draught, etc.) affected moss, and changes in toxicity exposure over time.

A.2 Moss Species Selection

Moss growing naturally on the island of Oahu was collected from areas uncontaminated by the metal of interest. Four (4) distinct varieties of moss were collected and placed in petri dishes with habitat-sourced clay soil as a base. These samples were tested over an eight-week period. The first moss was a light, small, bright green species found on Palm Tree (*Prichardia* variety) trunks. Shown in Figure A-3, it was initially found in significant quantities, had a reasonable water content (50%), and was easily removed making it a prime candidate. It was readily found in urban environments which offered opportunities to examine toxicity levels from more difficult to measure areas by other methods due to high runoff from concrete and asphalt.



Figure A-3: Moss attached to palm tree trunk.

Unfortunately, after eight (8) weeks the moss showed no notable growth. The introduction of excess water observed in and outside of our controlled growing environment appeared to negatively impact growth. Also, its abundance was adversely impacted by the onset of the wet season making the chance for collecting sufficient quantities throughout the long-term course of experimentation questionable.

The other samples (Figure A-4) were collected later from an area near the entrance to Wa’ahila Ridge Trail above St. Louis Heights (21.307°, -157.797°) and quickly transplanted to petri dishes. Each was distinguished by color and size, though there was some concern that size variation could impact the assurance of balanced application of metals. Physically larger varieties proved to have greater benefit of displaying measurable and definable change as a result of exposure.

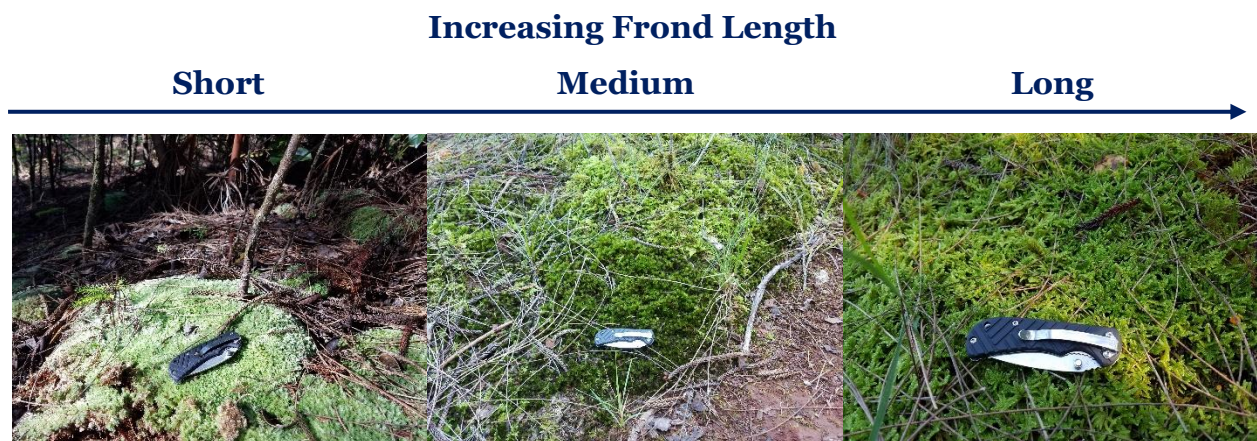


Figure A-4: Alternative moss specimen collected.

The shortest variety seems to grow upward building up on top of older layers. It was distinguished as being composed of 1-cm sections of puffed light green fronds radiating from a central stem structure. Older sections were denoted as being paler in coloration moving away from the green and taking on a pale-yellow coloration. There was possible indication that the

older sections could leave a more definitive environmental record, but no conclusive results returned from initial drying, powdering, and testing for atmospheric deposition of cesium from the most recent input after the Fukushima Daiichi Accident in 2011. As with any moss variety, it was uncertain how quickly the shorter specimen would grow, yet it was the muted coloration and ease of breaking that brought into question if the variety was robust enough for testing conditions.

The medium sized sample has a dark brown stem and root structure that gives way to a bright green plume at the top. It does not have a particularly large coverage compared to other varieties raising concerns about its viability as a test specimen. The darker coloration was also observed to be a potential negative as it could increase the difficulty in observing change either with the naked eye or with the laser.

The final long and frond-like moss (*Thuidium plicatile*; used in this paper) almost resembled a fern though not nearly as rigid. It has a browning discoloration in certain sections which could denote localized death or aging in the specimen. Though it was the only specimen tested using the laser apparatus to date, it was found that a single strand of the moss frond was sufficient for analysis. This suggests we could limit the fraction of moss extracted from our test sample. By limiting the mass extracted, smaller test samples would be needed, and the statistical impact of periodic sampling minimized. Regardless of the species selected, though, moss should survive without soil for prolonged periods and it was anticipated that some cellular death would occur even in a perfect environment.



Figure A-5:
Thuidium plicatile

Thuidium plicatile is a moss species indigenous to Hawai‘i (Staples et al., 2004) and the one chosen to be used for experimentation and observation. The specific specimen used was collected from O‘ahu along the Wa‘ahila Ridge Trail. A frond-like species in appearance, *Thuidium plicatile* is similar in appearance to the invasive *Hypnum plumaeforme* Wilson (Crum & Mueller-Dombois 1968; Hoe 1974) which is not recorded as being present on O‘ahu (Staples et al., 2004). *Thuidium plicatile* Mitt. and *Thuidium plicatile* Mitt. var. *brevifolium* E.B. Bartram are more broadly recognized as synonyms of *Thuidium cymbifolium* Dozy & Molk (Hoe 1974; Touw, 2001). *Thuidium* is the genus of moss in the family *Thuidiaceae* so named for the fronds appearing to look like small cedar trees with creeping, branching and pinnate leaves. 194 accepted names are known in the genus *Thuidium* with all species existing in temperate to tropical climates (The Plant List, 2013).

A.3 Moss Cultivation

After the collection or growth phase was complete, the specimen were distributed into four equally sized trays. Separate trays were available to provide separation between trials for each toxicity level. The trays were enclosed within a plastic sheet surrounding a PVC constructed frame. The materials are light and affordable allowing for removal and replacement between experiments and easier storage. The trays were accessed through a flap on the front of the frame that was opened only for wetting or sample removal to maintain internal environmental conditions. Full-spectrum grow lights were hung 0.5 m above the samples at low wattage to simulate the low light, shaded natural habitat where the moss was collected. The LED lights were chosen because they produce a full range of wavelengths, minimize power usage, do not generate significant heat, and are dimmable allowing for photoperiod simulation with an automatic timer. Ten (10) hours of light followed by night period of darkness provides enough light energy for photosynthesis and rest time for respiration to promote optimal growth.

The use of a heater was deemed a potential concern due to fluctuations in the laboratory's temperature. If the box environment is too cold, moss growth may slow and response to treatment metals may not be representative. However, the moss may dry out if the environment is too warm. To address this concern, a heating cable with a 110V rating and low 105W consumption was considered, but the enclosure normalized at a suitable temperature. To stabilize humidity between wetting, petri dishes were half filled with water and placed in each corner of the grow tent. There was also enough air within the tent and circulation from opening it each day that a small fan affixed in the bottom corner of the containment was not deemed necessary.

Leading up to the experiment the moss received a light misting of tap (groundwater) water every day to prevent drying out and to promote growth and natural humidity within the box. Once the experiment began all samples received either DI or DI+Cu outside of the housing environment and only returned after it had been through LIF imaging. Different spray bottles were used to simulate a misting rain effect for uniform coverage. Each trial had its own spray bottle solution from which 30 mL were dosed on treatment days. Only 30 mL of DI was given on all other days from the same spray bottle for all trials.

Appendix B – Normalization plots

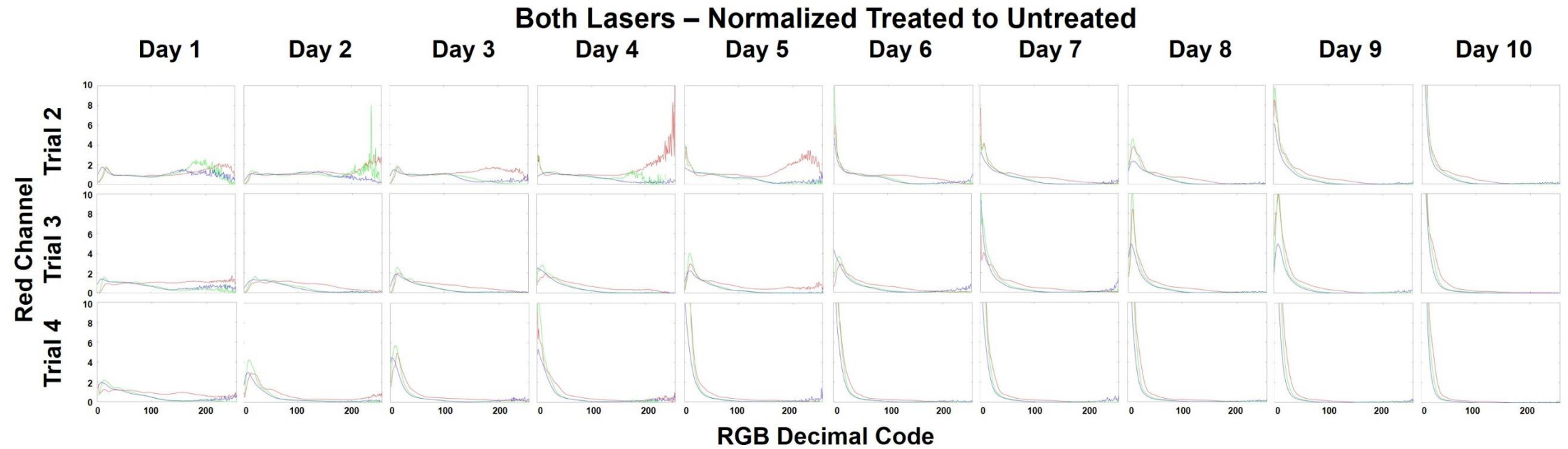


Figure B-1: Normalized plots (both lasers) using color channels generated from initial images and their histogram profiles (Figure 6). Each trial is normalized to the control (trial 1) to observe changes across the RGB decimal codes in each color channel.

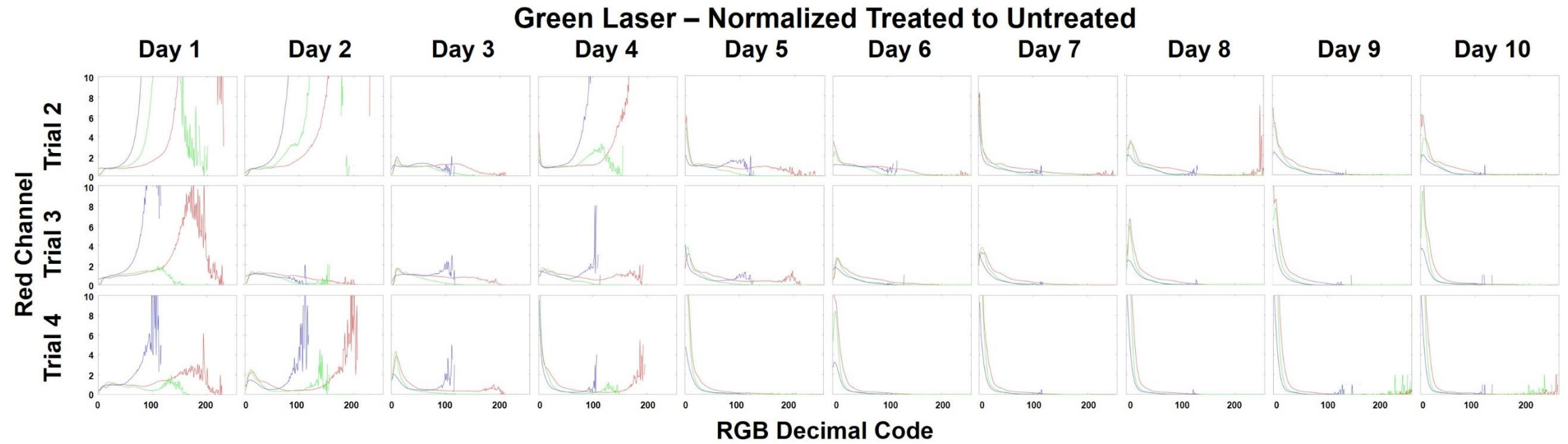


Figure B-2: Normalized plots (green laser only) using color channels generated from initial images and their histogram profiles (Figure 7). Each trial is normalized to the control (trial 1) to observe changes across the RGB decimal codes in each color channel.

Bibliography

- Berg, T., Steinnes E. (1997). Use of mosses (*Hylocomium splendens* and *Pleuroziumschreberi*) as biomonitors of heavy metal deposition: from relative to absolute deposition values. *Environmental Pollution*, 98, 61–71. [https://doi.org/10.1016/S0269-7491\(97\)00103-6](https://doi.org/10.1016/S0269-7491(97)00103-6)
- Berg, T., Røyset, O., Steinnes, E., & Vadset, M. (1995). Atmospheric trace element deposition: Principal component analysis of ICP-MS data from moss samples. *Environmental Pollution*, 88(1), 67–77. [http://doi.org/10.1016/0269-7491\(95\)91049-q](http://doi.org/10.1016/0269-7491(95)91049-q)
- Brumbaugh, W. G., Arms, J. W., Linder, G. L., & Melton, V. D. (2016). Development of ion-exchange collectors for monitoring atmospheric deposition of inorganic pollutants in Alaska parklands (No. 2016-5096). US Geological Survey.
- Carginale, V., Sorbo, S., Capasso, C., Trinchella, F., Cafiero, G., & Basile, A. (2004). Accumulation, localisation, and toxic effects of cadmium in the liverwort *Lunularia cruciata*. *Protoplasma*, 223, 53–61. <https://doi.org/10.1007/s00709-003-0028-0>
- Chakraborty, S., & Paratkar, G. T. (2006). Biomonitoring of trace element air pollution using mosses. *Aerosol and Air Quality Research*, 6, 247–258. <https://doi.org/10.4209/aaqr.2006.09.0002>
- Chen, Y. E., Yuan, S., Su, Y. Q., & Wang, L. (2010). Comparison of heavy metal accumulation capacity of some indigenous mosses in Southwest China cities: a case study in Chengdu city. *Plant, Soil and Environment*, 56(No. 2), 60–66. <https://doi.org/10.17221/160/2009-pse>
- Choudhury, S., & Panda S. K. (2005): Toxic effects, oxidative stress and ultrastructural changes in moss *Taxithelium nepalense* (Schwaegr.) Broth. under chromium and lead phytotoxicity. *Water, Air, Soil Pollution*, 167, 73–90. <https://doi.org/10.1007/s11270-005-8682-9>
- Colman, J. A., Rice, K. C., & Willoughby, T. C. (2001). Methodology and significance of studies of atmospheric deposition in highway runoff. Open-File Report 01-259. *US Geological Survey, Northborough, Massachusetts*. <https://pubs.usgs.gov/of/2001/ofr01-259/pdf/ofr01259.pdf>
- Crum, H., & Mueller-Dombois, D. (1968). Two new mosses from Hawaii. *Journal of the Hattori Botanical Laboratory*, 31, 293–296. <https://doi.org/10.11646/bde.25.1.7>
- Ćujić, M., Dragović, S., Sabovljević, M., Slavković-Beškoski, L., Kilibarda, M., Savović, J., & Onjia, A. (2013). Use of Mosses as Biomonitors of Major, Minor and Trace Element Deposition Around the Largest Thermal Power Plant in Serbia. *CLEAN - Soil, Air, Water*, 42(1), 5–11. <https://doi.org/10.1002/clen.201100656>
- Degola, F., De Benedictis, M., Petraglia, A., Massimi, A., Fattorini, L., Sorbo, S., Basile, A., & di Toppi, L. S. (2014). A Cd/Fe/Zn responsive phytochelatin synthase is constitutively present in the ancient liverwort *Lunularia cruciata* (L.) Dumort. *Plant and Cell Physiology*, 55, 1884–1891. <https://doi.org/10.1093/pcp/pcu117>
- Fatoba, P. O., Ogunkunle, C. O., Oyedeji, S., & Salawudeen, M. B. (2013). Heavy Metal Depositions around some Petroleum Product Depots in Nigeria, using Mosses as Biomonitors. *The Bioscientist Journal*, 1(1), 99-105. https://bioscientistjournal.com/index.php/The_Bioscientist/article/view/26

- Figueira, R., Sérgio, C., & Sousa, A. J. (2002). Distribution of trace metals in moss biomonitors and assessment of contamination sources in Portugal. *Environmental Pollution*, 118(1), 153–163. [https://doi.org/10.1016/s0269-7491\(01\)00203-2](https://doi.org/10.1016/s0269-7491(01)00203-2)
- García-Sánchez, F., Galvez-Sola, L., Martínez-Nicolás, J. J., Muelas-Domingo, R., & Nieves, M. (2017). *Using Near-Infrared Spectroscopy in Agricultural Systems. Developments in Near-Infrared Spectroscopy*. <https://doi.org/10.5772/67236>
- Gatzolis, Demetrios, Jovan, Sarah, Donovan, Geoffrey, Amacher, Michael, Monleon, Vicente (2016). Elemental atmospheric pollution assessment via moss-based measurements in Portland, Oregon. *Gen. Tech. Rep. PNW-GTR-938*. Portland, OR: U.S. Department of Agriculture, Forest Service, Pacific Northwest Research Station. <https://www.fs.usda.gov/treearch/pubs/51076>
- González, A. G., & Pokrovsky, O. S. (2014). Metal adsorption on mosses: toward a universal adsorption model. *Journal of Colloid and Interface Science*, 415, 169–178. <https://doi.org/10.1016/j.jcis.2013.10.028>
- Hoe, W.J. (1974). Annotated checklist of Hawaiian mosses. *Lyonia*, 1(1): 1–45. <http://hdl.handle.net/10125/10729>
- Mehran Hoodaji, Mitra Ataabadi & Payam Najafi (2012). Biomonitoring of Airborne Heavy Metal Contamination, Air Pollution. *Monitoring, Modelling, Health and Control*. Mukesh Khare. IntechOpen. <http://doi.org/10.5772/32963>. Available from: <https://www.intechopen.com/books/air-pollution-monitoring-modelling-health-and-control/biomonitoring-of-airborne-heavy-metal-contamination>
- Jekel, C. F., Venter, G., Venter, M. P., Stander, N., & Haftka, R. T. (2018). Similarity measures for identifying material parameters from hysteresis loops using inverse analysis. *International Journal of Material Forming*. <https://doi.org/10.1007/s12289-018-1421-8>
- Kinsey, J. L. (1977). Laser-Induced Fluorescence. *Annual Review of Physical Chemistry*, 28(1), 349–372. <https://doi.org/10.1146/annurev.pc.28.100177.002025>
- Koz, B., Cevik, U., & Akbulut, S. (2012). Heavy metal analysis around Murgul (Artvin) copper mining area of Turkey using moss and soil. *Ecological Indicators*, 20, 17–23. <https://doi.org/10.1016/j.ecolind.2012.02.002>
- Koz B., & Cevik U. (2014). Lead adsorption capacity of some moss species used for heavy metal analysis. *Ecological Indicators*, 36, 491–494. <https://doi.org/10.1016/j.ecolind.2013.08.018>
- Krzyszowska, M. (2011). The cell wall in plant cell response to trace metals: polysaccharide remodeling and its role in defense strategy. *Acta Physiologiae Plantarum*, 33, 35–51. <https://doi.org/10.1007/s11738-010-0581-z>
- Krzyszowska, M., Rabeda, I., Lewandowski, M., Samardakiewicz, S., Basinska, A., Napieralska, A., Mellerowicz, E.J., & Woznyl, A. (2013). Pb induces plant cell wall modifications – in particular – the increase of pectins able to bind metal ions level. *E3S Web of Conferences*, 1(26008). <https://doi.org/10.1051/e3sconf/20130126008>
- Maarek, J.I. & Kim, S. (2001). Multispectral excitation of time-resolved fluorescence of biological compounds: variation of fluorescence lifetime with excitation and emission wavelengths. *Proc SPIE*, 4252,124–131. <https://doi.org/10.1117/12.426734>

- Misra, A. K., Acosta-Maeda, T. E., Sandford, M., Gasda, P. J., Porter, J. N., Sharma, S. K., ... Egan, M. J. (2018). Standoff Biofinder: powerful search for life instrument for planetary exploration. *Lidar Remote Sensing for Environmental Monitoring XVI*. <https://doi.org/10.1117/12.2324201>
- Misra, A. K., Acosta-Maeda, T. E., Sharma, S. K., McKay, C. P., Gasda, P. J., Taylor, G. J., ... Wiens, R. (2016). "Standoff Biofinder" for Fast, Noncontact, Nondestructive, Large-Area Detection of Biological Materials for Planetary Exploration. *Astrobiology*, *16*(9), 715–729. <https://doi.org/10.1089/ast.2015.1400>
- Nagajyoti, P. C., Lee, K. D., & Sreekanth, T. V. M. (2010). Heavy metals, occurrence and toxicity for plants: a review. *Environmental Chemistry Letters*, *8*, 199–216. <https://doi.org/10.1007/s10311-010-0297-8>
- Onianwa, P. C. (2001). Monitoring atmospheric metal pollution: a review of the use of mosses as indicators. *Environmental Monitoring and Assessment*, *71*, 13–50. <https://doi.org/10.1023/A:1011660727479>
- Pan, Y. P., & Wang, Y. S. (2015). Atmospheric wet and dry deposition of trace elements at 10 sites in Northern China. *Atmospheric Chemistry & Physics*, *15*(2). <http://doi.org/10.5194/acp-15-951-2015>
- Reinfelder, J. R., Totten, L. A., Eisenreich, S. J., & Aucott, M. (2005). Research Project Summary. *New Jersey Atmospheric Deposition Network (April, 2005)*. https://www.nj.gov/dep/dsr/nutrients/NJ%20Atmospheric%20Deposition%20Network_RPS.pdf
- Reski, R. (1998): Development, genetics and molecular biology of mosses. *Botanica Acta*, *111*, 1–15. <https://doi.org/10.1111/j.1438-8677.1998.tb00670.x>
- Ryan, G. F. (1977). Controlling Mosses and Liverworts. *Breeders Roundtable in Eugene, Oregon*. Western Washington Research and Extension Center. Retrieved from <https://scholar.lib.vt.edu/ejournals/JARS/v32n2/v32n2-ryan.htm>
- Shakya, K., Chettri, M. K., & Sawidis, T. (2008). Impact of heavy metals (copper, zinc, and lead) on the chlorophyll content of some mosses. *Archives of Environmental Contamination and Toxicology*, *54*, 412–421. <https://doi.org/10.1007/s00244-007-9060-y>
- Stanković, J. D., Sabovljević, A. D., & Sabovljević, M. S. (2018). Bryophytes and heavy metals: a review. *Acta Botanica Croatica*, *77*(2), 109–118. <https://doi.org/10.2478/botcro-2018-0014>
- Staples, G.W., Imada, C.T., Hoe, W.J., & Smith, C.W. (2004). A revised checklist of Hawaiian mosses. *Tropical Bryology*, *25*, 35–69. <https://doi.org/10.11646/bde.25.1.7>
- Sun, S. Q., He, M., Cao, T., Zhang, Y. C., & Han, W. (2009). Response mechanisms of antioxidants in bryophyte (*Hypnum plumaeforme*) under the stress of single or combined Pb and/or Ni. *Environmental Monitoring and Assessment*, *149*, 291–302. <https://doi.org/10.1007/s10661-008-0203-z>
- Swain, M. J., & Ballard, D. H. (1992). *Indexing via Color Histograms*. *Active Perception and Robot Vision*, 261–273. https://doi.org/10.1007/978-3-642-77225-2_13

- Tan, J. Y., Ker, P. J., Lau, K. Y., Hannan, M. A., & Tang, S. G. H. (2019). *Applications of Photonics in Agriculture Sector: A Review. Molecules, 24(10), 2025.* <https://doi.org/10.3390/molecules24102025>
- The Plant List (2013). Version 1.1. Published on the Internet: <http://www.theplantlist.org/> (accessed 21st June).
- Touw, A. (2001). A taxonomic revision of the *Thuidiaceae* (Musci) of tropical Asia, the western Pacific, and Hawaii. *Journal of the Hattori Botanical Laboratory, 91, 1–136.* https://doi.org/10.18968/jhbl.91.0_1
- Tremper, A. H., Agneta, M., Burton, S., & Higgs, D. E. (2004). Field and laboratory exposures of two moss species to low level metal pollution. *Journal of Atmospheric Chemistry, 49, 111–120.* <https://doi.org/10.1007/s10874-004-1218-7>
- Vázquez, M. D., Lopez, J., & Carballeira, A. (1999). Uptake of heavy metals to the extracellular and intracellular compartments in three species of aquatic bryophyte. *Ecotoxicology and Environmental Safety, 44, 12–24.* <http://doi.org/10.1006/eesa.1999.1798>
- Velea, T., Gherghe, L., Predica, V., & Krebs, R. (2009). Heavy metal contamination in the vicinity of an industrial area near Bucharest. *Environ Sci Pollut Res 16, 27–32.* <https://doi.org/10.1007/s11356-008-0073-5>
- Wahsha, M., Bini, C., Fontana, S., Wahsha, A., & Zilioli, D. (2012). Toxicity assessment of contaminated soils from a mining area in Northeast Italy by using lipid peroxidation assay. *Journal of Geochemical Exploration, 113, 112–117.* <https://doi.org/10.1016/j.gexplo.2011.09.008>
- Wessel, Paul (2018). *Introduction to Statistics and Data Analysis.* University of Hawaii at Manoa, SOEST. ebook: <http://www.soest.hawaii.edu/wessel/DA/index.html>
- Wolterbeek, B. (2002). Biomonitoring of trace element air pollution: principles, possibilities and perspectives. *Environmental Pollution, 120, 11–21.* [https://doi.org/10.1016/S0269-7491\(02\)00124-0](https://doi.org/10.1016/S0269-7491(02)00124-0)
- Yang-Er, C., Zhong-Wei, Z., Ming, Y., & Shu, Y. (2019). Perspective of Monitoring Heavy Metals by Moss Visible Chlorophyll Fluorescence Parameters. *Frontiers in Plant Science, 10(35).* <https://doi.org/10.3389/fpls.2019.00035>
- Zare, R. N. (2012). My Life with LIF: A Personal Account of Developing Laser-Induced Fluorescence. *Annual Review of Analytical Chemistry, 5(1), 1–14.* <https://doi.org/10.1146/annurev-anchem-062011-143148>
- Zschau, T., Getty, S., Gries, C., Ameron, Y., Zambrano, A., & Nash, T. H. (2003). *Historical and current atmospheric deposition to the epilithic lichen Xanthoparmelia in Maricopa County, Arizona. Environmental Pollution, 125(1), 21–30.* [https://doi.org/10.1016/s0269-7491\(03\)00088-5](https://doi.org/10.1016/s0269-7491(03)00088-5)
- Zvereva, E. L., & Kozlov, M. V. (2011). Impacts of industrial pollutants on bryophytes: a meta-analysis of observational studies. *Water, Air & Soil Pollution, 218, 573–586.* <https://doi.org/10.1007/s11270-010-0669-5>